POLITECNICO DI MILANO
Corso di Laurea Magistrale in Ingegneria Energetica
Dipartimento di Energia
Scuola di Ingegneria Industriale e dell'Informazione

Numerical Analysis of Stratified Two-phase Flow in Horizontal Pipes using VOF Model

Supervisors:
Prof. Luigi P.M. Colombo
Prof. Riccardo Mereu

Samar Bahman 850518

Academic Year 2018-2019

Abstract

The main focus of the present work is the validation of the numerical simulation of two-phase stratified flow in horizontal pipes. Numerical simulations are performed using a 3D numerical domain coupled to a two-equation turbulence RANS model (SST k-ω) and interface tracking method Volume of Fluid (VOF) in adiabatic operating conditions at several superficial gas and liquid velocities (i.e., several void fraction values). Numerical results are in agreement with the experimental data collected at Politecnico di Milano showing a more significant difference at high superficial gas velocity with mean absolute percentage error (MAPE) of around 29% on pressure gradient prediction. The comparison includes global quantities (e.g., pressure gradient) and visual behavior (e.g., the shape of the interface) confirming the capability of the numerical model to catch the main characteristics of the stratified fluid flow. Moreover, a sensitivity analysis is conducted, taking into account the density of moist air and a mesh refinement at the interface. Numerical results showed an improved agreement with experiments where the difference between gas and liquid superficial velocities was significant.

Furthermore, wavy flow is simulated adopting the same sensitivity analysis done for the stratified flow.

Keywords: Numerical Simulation; Computational Fluid Dynamics [CFD]; Volume of Fluid Method [VOF]; Two-phase Flow; Stratified Flow; Horizontal Pipes; Pressure Gradient; Interface

Acknowledgements

I would like to express my special thanks of gratitude to my Professor Luigi P.M. Colombo for not only inspiring my interest in the field of multiphase flow systems and technologies but also giving me this golden opportunity to work on a research subject in which I was interested. Furthermore, I would like to thank my supervisor Professor Riccardo Mereu whose advice and help was a valuable asset in my progress in this project. Moreover, I am incredibly grateful for the assistance of Stefano Passoni during the period of this project, who helped me in solving my doubts with patience and wisdom.

Lastly, my sincerest thanks go to my mother, Shahzad Talakar, without whose support and encouragement the completion of this thesis was not possible.

Contents

List of Figures

List of Tables

Chapter 1

Introduction to Two-phase Flows: A Literature Review

1.1 Stratified Smooth Flow

Multiphase flow regimes can be grouped into the categories of gas-liquid, liquid-liquid flows, gas-solid flows, liquid-solid flows, and three-phase flows. The horizontal gas-liquid flows can be classified into seven groups according to their flow patterns as shown in Figure (1.1).
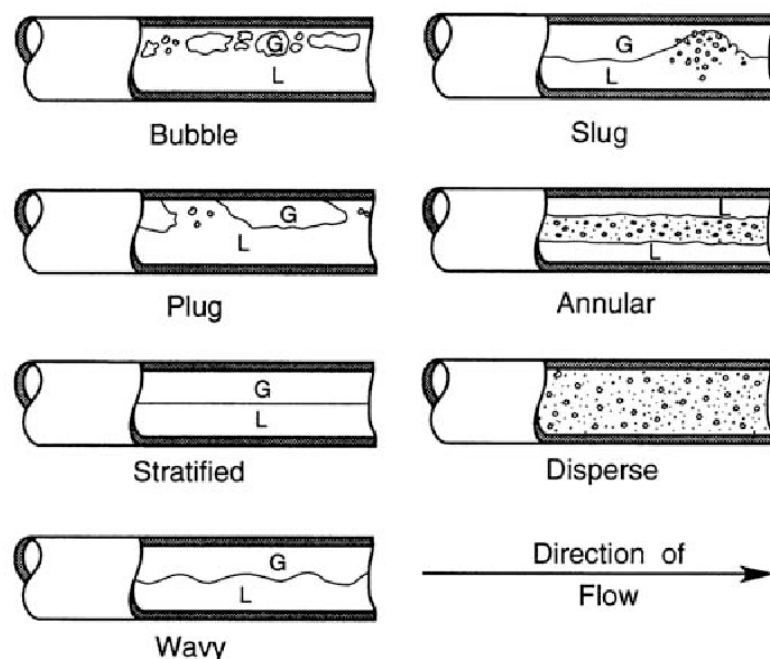
Figure (1.1)   Horizontal Two-phase Flow Patterns

Two-phase stratified flow is the flow of immiscible fluids separated by a clearly-defined interface which is frequently encountered in many industrial applications such as oil and gas, nuclear reactor cooling system, and geothermal plants, to mention a few. This flow is the most desirable

1

flow regime for the oil and gas industry since it creates a low pressure drop, less erosion and equipment failure, and facilities easier phase separation.

Stratified gas-liquid flow is the dominating two-phase combination inside transportation pipelines and is mainly present as a gas-condensate or gas-water mixture. The condensation of natural gas is an inevitable process that occurs due to the temperature and pressure changes that are imposed on the pipes by the natural surroundings. In offshore gas fields, the raw production is often transported in multiphase pipelines before it reaches a processing unit. These lines are at the bottom of the sea in horizontal and near-horizontal positions. Hence, a better understanding of the flow characteristics of stratified gas-liquid flow in horizontal pipes is needed for the proper design and operation of pipelines that are subjected to stratified flows.

The effects of the flow on the quantities such as flow rate, pressure drop, and flow regimes, have always been of engineering interest. Wallis and Dobson (1973) analyzed the onset of gas-liquid slug or plug flow in rectangular horizontal and near-horizontal ducts. Taitel and Dukler (1976) introduced a prediction of horizontal flow regime transitions in pipes. They elaborately discussed and developed correlations for the transition between stratified smooth, stratified wavy, intermittent (slug and plug), dispersed bubble, and annular dispersed liquid flow considering pipe size, fluid properties, and angle of inclination.
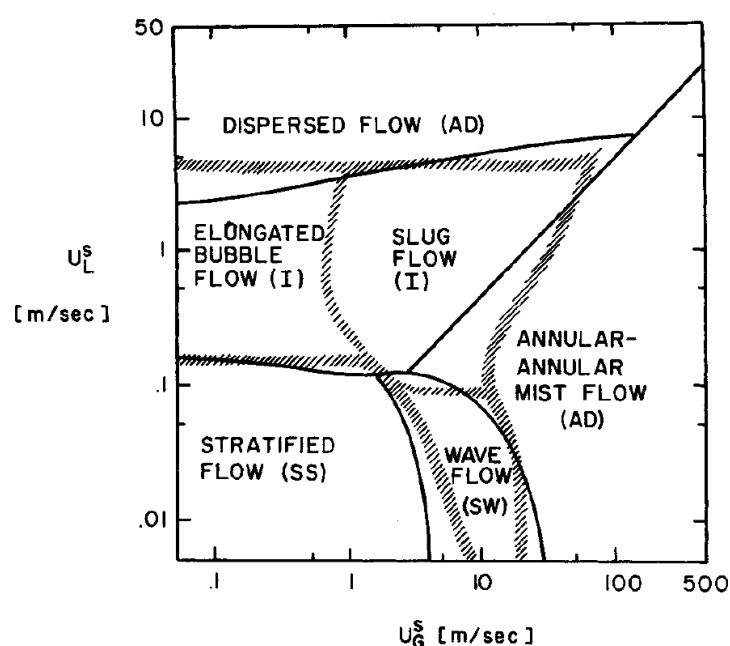
Figure (1.2)   Taitel and Dukler Obtained Results Comparison with Experiments

Stratified two-phase flow is a flow regime that occurs when the velocity of each phase is relatively low. In such flows, the inertia forces are not large enough to generate large waves that may lead to the onset of intermittent flow regimes such as slug flow or dispersed flow, which are considered as more complicated and problematic in industrial contexts. Sanchis et al. (2011) reported on how stratified flow can develop into hydrodynamic slugging through wave interaction. They developed an interface tracking technique to measure the characteristics of two-phase stratified flow accurately. They compared their experimental results with viscous Kelvin-Helmoltz stability theory finding that this method fails to predict the occurrence of slugging for their experimental tests.

The interfacial wave generated by the slip ratio between the gas and liquid superficial velocity strongly affects the character of the flow, which indicates the significant effect of the presence of interfacial wave on the pressure drop.

Estimation of pressure drop and liquid hold-up are limited to one-dimensional mechanistic modeling, where the shear stress in the interface are calculated based on the average velocity. There is a critical need to conduct CFD simulations to predict the liquid structure and gas-liquid interface in detail. The CFD simulation can help to study multiphase stratified flow at any interface within the system reliability and in a cheaper way.

Computational fluid dynamics (CFD) techniques have been used to simulate the stratified pipe flow. One of the early CFD models of turbulent stratified flow in a horizontal pipe was presented by Shoham and Taitel (1984), where a 2D simulation for liquid-gas flow was simulated by adopting zero-equation models for the liquid region flow field while the gas region was treated as bulk flow. Shoham and Taitel (1984) applied the combination of 2D momentum equation and eddy viscosity turbulence model to characterize the liquid phase behavior in stratified flow. For the gas phase, the gas and interface stresses are estimated based on the bulk flow calculations. Their model was able to predict the liquid velocity field, hold-up, and pressure drop, given the gas and liquid flow rates, physical properties, pipe size, and inclination angle. So a better model for stratified flow was developed rather than the Lockhart and Martinelli's.

Issa et al. (1988) combined the momentum equation for gas and liquid with k-ε model and modeled the fully-developed stratified flow, applying wall function for solid boundaries. Their method includes two versions of the k-ε turbulence model, for high and low Reynolds numbers. Their al-

gorithm is based on the solution of basic governing differential equations numerically, using a finite element technique, and a curvilinear orthogonal mesh which caters for both rectangular and circular cross-sections. This algorithm solves the set of finite-difference equations in an iterative loop, in which the equations are solved sequentially. The results were in close agreement with Taitel and Dukler mechanistic model.

Advances in computational fluid mechanics have provided the basis for further insight into the dynamics of multiphase flows. Currently, there are two approaches for the numerical calculation of multiphase flows: the Euler-Lagrange approach and the Euler-Euler approach.

In the Euler-Euler approach, the different phases are treated mathematically as inter-penetrating continua. Since the other phases can not occupy the volume of a phase, the concept of phasic volume fraction is introduced. These volume fractions are assumed to be continuous functions of space and time, and their sum is equal to one. Conservation equations for each phase are derived to obtain a set of equations, which have a similar structure for all phases. These equations are closed by providing constitutive relations that are obtained from empirical information.

Various multi-dimensional numerical models were developed to simulate stratified flows:

- Harlow and Welch (1965) developed a method called Marker and Cell, where they wrote the finite difference form of full Navier-Stokes equations for a time-dependent incompressible flow. Their new method considers marker particles whose trajectories follow the motion of elements throughout the fluid. These particles are placed in the fluid containing cells initially and are moved with the local velocity. Finally, a linear interpolation is used to calculate the velocity with which a particle should move. Although simple, this method requires ample computer storage and additional computational time.

- Lagrangian grid methods and Volume of Fluid method discussed by Hirt and Nichols (1981) introduced a function whose value is unity at any point occupied by the fluid and zero otherwise, and the average of this function indicated the fractional volume of the cell occupied by the fluid. The VOF model requires minimum storage requirements and follows the interface more accurately.

- The level set method was presented by Sussman (1994) that implicitly captures the interface instead of explicitly tracking the interface.

> A new function is defined as the signed normal distance from the interface. This method is computationally affordable as it can be used for coarse meshes.

These methods are, in principle, able to accurately capture most of the physics of the stratified flows. However, they cannot capture all the morphological formations like small bubbles and droplets if the grid is not reasonable small enough.

Newton and Behnia (2000) obtained excellent agreement with experimental results for stratified pipe flow by employing a low Reynolds number k-ε turbulent model for turbulent viscosity instead of wall functions which incorporated wall damping functions obtained from single-phase pipe flow.

One of the first attempts to simulate mixed flows was presented by Cernea et al. (2001), who coupled the VOF method and interface reconstruction algorithms with a two-fluid model in order to bring together the advantages of both analytical formulations and investigate the interface tracking grid dependence. Banerjee and Isaac (2003) applied CFD code to simulate stratified flow by using the VOF model and three different turbulent models, namely standard k-ε, RNG k-ε, and Reynolds Stress Model. The results show that standard k-ε and RNG k-ε turbulence models give a closer match to the experimental results, however, RNG k-ε turbulence model gives overall best results compared to the other models.

De-Sampaio et al. (2008) applied the k-ω model turbulence model and Newton-Raphson Scheme to solve the Reynolds averaged Navier-Stokes equations for modeling the gas-liquid stratified model. Results were compared to the Taitel and Dukler model, indicating that k-ω turbulent model is suitable for numerical simulation of such flows; however, a better understanding of imposing interfacial values for k and ω is required to obtain a better agreement with experimental data of stratified wavy two-phase flow. Sisi-Ali and Gatingnol (2008) developed a CFD simulation with the k-ε turbulence model to model the stratified flow with and without gravity effect. They investigated the velocity profile, pressure and turbulent quantities of the phases as well as the phase distribution. In case of profiles of phases, densities, velocities, turbulent kinetic energies, and dissipation rates, the results show a clean separation between the two phases by an interface that affects all these quantities. Pressure increases for the flow with gravity in the liquid until the bottom

of the channel, while the pressure is constant in the air as in the liquid for the case without gravity. The highest value of the velocity of water is seen at the interface. The maximum turbulent kinetic energy is seen for the flow with gravity. The maximum of turbulence dissipation rate is obtained at the upper wall and the minimum at the interface.

Hui et al. (2003) numerically simulated stratified oil-water two-phase turbulent flow in a horizontal tube using a VOF model. An acceptable agreement with experimental data was achieved for the predictions of pressure loss and slip ratio. They applied the RNG k-ε model combined with a near-wall low-Re turbulence model to each phase, and they adopt continuum surface force approximation for the calculation of surface tension. Although the predicted local phase fraction profile showed excellent agreement with experimental results, the prediction of the velocity field was only satisfactory. Carlos F. (2006) developed a 2D model for fully developed, turbulent-turbulent oil-water stratified flow using the finite-volume method in a bipolar coordinate system and applying a simple mixing-length turbulence model. The predictions of the proposed model for the flow velocity fields of both phases showed a satisfactory agreement when compared with experimental data. Al-Yaari et al. (2011) simulated oil-water two-phase turbulent flow in a horizontal pipe volume of fluid (VOF) model and adopting the RNG k-ε turbulence model. CFD Numerical simulation predicted the stratified flow pattern and smoothness and the type of the interface. On the other hand, while the CFD model accurately predicated the oil layer, the water layer was not predicted as a segregated layer.

Dabirian et al. (2015) conducted a CFD simulation of the air-water horizontal pipeline using ANSYS Fluent. The Volume of Fluid (VOF) model was used as a multiphase flow model, and the Realizable k-ε model with standard wall functions is employed as the turbulent model. They investigated several parameters such as liquid hold-up, which was in good agreement with experimental results; however, a poor agreement was obtained by comparing with the Taitel and Duckler (1976) model. Nevertheless, a satisfactory agreement was achieved for the wall shear stress on the gas side compared to the Taitel and Duckler (1976) model.

1.2   Stratified Wavy Flow

Despite its relative simplicity, stratified flow is still far from completely understood due to its complex underlying physics. In a co-current gas-liquid flow, where the gas moves faster than the liquid-layer beneath it, the waves that were initially induced upstream by interfacial shear forces will be perceived, by the gas-phase, as a slowly moving deformed surface locally. This will, in turn, influence the flow conditions of the gas and consequently change the interfacial shear downstream. Hence, two-way interaction between the flow dynamics, or more specifically, the dynamics of turbulent structures of each phase and local interface morphology is created.

The work of Lockhart and Martinelli (1949) and Andritsos and Hanratty (1987) more focused on the measurement of the superficial velocity, pressure drop, and liquid hold-up and proposing empirical correlation to predict the pressure drop based on experimental data. Strand (1993) and Espedal (1998) used more advanced measurements of the wavefields by employing conducting probes and Fernandino and Ytrehus (2006) used the more complicated technique of Laser Doppler Velocimetry (LDV). Analyzing the spectral cross-correlation output, it was established that the stratified flow regime consists of a range of well-defined sub-regimes determined by the interfacial wave kinematics.

Espedal (1998) divided them into the following five regions:

1. Smooth flow: No waves were observed.

2. Small Amplitude Waves I: Amplitudes below 2 mm and wave lengths between 2 and 6 cm. The power spectrum showed no peak at all or one peak.

3. Small Amplitude 2D Waves II: Similar to the waves above, but the power spectrum showed two peaks.

4. Large Amplitude 2D Waves: Amplitudes above 2 mm, and the waves are less regular. The power spectrum has a one, two, or no marked peaks.

5. Large Amplitude 3D Waves: Amplitudes above 2 mm, and the waves do not have a two-dimensional shape.

Moreover, it is common knowledge that interfacial turbulence structures are responsible for not only the scalar mixing (mass, momentum,

temperature, energy, etc.) between phases but also for the pressure drop along the pipe as they enhance the overall shear friction of the flow. Therefore, a better understanding of the relation between the different stratified flow patterns and their belonging turbulence dynamics might be the key to more accurate mathematical modeling. However, details about the turbulent structures near the gas-liquid interface are difficult to access using conventional instrumentation. Fabre et al. (1987) presented successful LDA measurements of turbulence parameters close to the interface of wavy stratified flow where the results showed an important mean secondary flow in the cross-section as well as an asymptotic behavior of the mean velocity and Reynolds stress components near the interface.

The prediction of pressure drop, average hold-up, and velocities has traditionally been based on a greatly simplified representation of the flow where both phases are treated as one-dimensional bulk flows, also called the two-fluid 1D model such as the work of Ullmann and Brauner (2006). However, the application of this model in a stratified flow relies on the availability of closure relations for the wall and interface shear stress. These closure relations depend on system parameters (e.g., fluid properties, pipe characteristics, etc.) and flow-related parameters in both phases. In the most common approaches, empirical correlations for the interfacial friction factors are obtained from experimental data, highlighting the importance of the experimental aspect within this field.

Bartoseiwicz et al. (2006) applied the VOF to find wave celerity, critical wave number, and also the transition between stratified smooth and wavy. Good agreements have been achieved between the experimental data and CFD predictions by taking into account the surface tension as a primary parameter in terms of dynamics growth.

Holmas et al. (2005) employed CFD to find the characteristics of stratified flow in a horizontal channel by the VOF model. Two turbulent models, namely RNG k-ε and MSST k-ω, were employed with particular attention to the turbulence near the gas-liquid interface. They compared the predicted velocity and kinetic energy profiles with the experiments by Akai et al. (1980) for a smooth interface and by Lorencez et al. (1997) for a wavy interface. In both cases, the gas and liquid flow rates disagreed with the experimental results. Hence, it was concluded that a correction for the turbulence is required.

Terzouli et al. (2008) performed CFD calculations of a two-dimensional domain, and their results showed that the three-dimensional effects are

not negligible so that 2D simulations are not suitable to correctly predict the stratified fluid flow. They conducted single-phase analyses as well using Fluent and ANSYS CFX to compare 2D and 3D simulations for both air and water single-phase domains. They achieved relevant improvements in both water and air velocity profiles with 3D simulations.

Lo and Tomasello (2010) investigated the capability of STAR-CD to simulate multiphase gas-liquid flow in pipelines using the VOF method coupled with the RANS equations. They examined two methods for the treatment of the interface in stratified flow without an interface reconstruction algorithm. The results show that the damping of turbulence at the interface is necessary to predict the correct pressure losses and liquid levels. This is achieved by using a damping coefficient in front of the turbulent viscosity or adding a source term in the energy dissipation equation. However, mesh independence should be investigated for both of these methods. Besides, this correction is only effective when strong velocity gradients are detected.

Chinello (2014) developed a RANS code to simulate gas-liquid turbulent stratified flow between two flat plates using k-ω Low Reynolds correction model. The k-ω model was modified to correctly predict the turbulence at the gas side of the interface. Good agreement with experimental results was observed for the stratified smooth case, while less satisfactory results were obtained for the stratified wavy case. Nonetheless, the stratified wavy case results were in agreement with the experiments. Furthermore, mesh refinement at the interface showed more satisfactory results.

Ali (2017) performed in-depth research simulating both stratified and intermittent flow using the Volume of the Fluid (VOF) model. Different turbulent models were used to simulate the stratified flow namely standard k-ε, standard RNG k-ε, differential RNG k-ε, and k-ω model. The best results were obtained by the differential RNG k-ε model. The results suggest reducing the turbulent kinetic energy generation in the simulations. Moreover, the difference between experimental and numerical results was attributed to the nature of the VOF formula since it calculates the flow field around the interface based on the physical properties of the mixture.

Chinello et al. (2019) presented the first study to investigate the performance of CFD with the VOF method, with and without damping at the interface. They compared the simulation results with experimental results for the pressure drop, the liquid hold-up, and the velocity PIV as

well as for the characteristics of the waves for stratified gas-liquid flow in pipes. Their main finding was that while bulk quantities such as the pressure drop and hold-up can be predicted very accurately (up to $\pm10\%$), when turbulence is damped at the gas-liquid interface, the prediction of the velocity profiles and of the wave characteristics is unsatisfactory both with and without turbulence damping at the interface.

The present work focuses on the numerical analysis of the adiabatic two-phase stratified smooth and stratified wavy flows with a concentration on investigating pressure drop and interface shape. Numerical simulation of the operating conditions in a lower range of gas superficial velocities is poorly studied in the literature, but significant for the application to gas flow lines. The aim is to reach a better agreement with the experimental data by applying the modifications in the literature to the simulation models and conducting different sensitivity analysis. The simulations were performed using a 3D numerical domain coupled with k-ω SST turbulence RANS model and the Volume of Fluid (VOF) interface tracking model. Numerical results were compared to the experiments conducted in Multiphase Thermo-Fluid Dynamics Laboratory at Politecnico di Milano. The preliminary numerical results show a good agreement with experimental data for stratified smooth flow. Moreover, the effect of air density and further mesh refinement at the interface was investigated for stratified smooth flow. As a result, a simulation case was developed for further examination of stratified wavy flow.

Chapter 2

Governing Equations

The purpose of this chapter is to elaborate on the governing equations used for simulation of the two-phase stratified flow. In this chapter Navier-Stokes Continuity and Momentum Equations, k-ω Turbulence Model, and Volume of Fluid Method are described in detail.

2.1 Continuity and Momentum Equations

The equation for conservation of mass, or continuity equation, can be written as follows:

$$\frac{\partial \rho}{\partial t} + \nabla . (\rho \vec{v}) = 0 \tag{2.1}$$

Conservation of momentum in an inertial (non-accelerating) reference frame is described by

$$\frac{\partial}{\partial t} (\rho \vec{v}) + \nabla . (\rho \vec{v} \vec{v}) = -\nabla p + \nabla . (\bar{\tau} + \bar{\tau}_t) + \rho \vec{g} + \vec{F} \tag{2.2}$$

where p is the static pressure, $\rho \vec{g}$ is the gravitational body force, and $\vec{F}$ is an external force term that can be used to model the effect of surface tension. The molecular stress tensor, $\bar{\tau}$, in Equation (2.2) is defined as

$$\bar{\tau} = \mu \left[\left(\nabla \vec{v} + \nabla \vec{v}^T \right) - \frac{2}{3} \nabla . \vec{v} I \right] \tag{2.3}$$

The turbulent stress tensor (Reynolds Stress) in Equation(2.2) is defined as

$$\bar{\tau}_t = \mu_t \left[\left(\nabla \vec{v} + \nabla \vec{v}^T \right) - \frac{2}{3} \left(\nabla . \vec{v} + \rho k \right) I \right] \tag{2.4}$$

in which I is the unit tensor.

2.2   Turbulence Model

There are numerous methods to model the turbulence; however, specific types of modeling are more practical in the specific case of two-phase stratified flow. The largest family of models in the field of turbulence is Reynolds-Averaged Navier-Stokes Models (RANS), which uses viscosity terms to close the turbulence equations. Among all the models in this family, k-ε and k-ω models are of much more interest in the field of two-phase stratified flows.

In the case studied here, the k-ω model was used to model the turbulence of the two-phase stratified flow. Hence, only this model is described in detail in this section.

2.2.1   k-ω Models

Standard k-ω Model

Turbulent kinetic energy (TKE) is defined as the mean kinetic energy per unit mass associated with the eddies in turbulent flow. Physically, the turbulence kinetic energy is characterized by measure root-mean-square (RMS) velocity fluctuations. Generally, the TKE is defined as the half of the sum of the variances (square root standard deviation) of velocity components:

$$k = \frac{1}{2} \left(\overline{(u')^2} + \overline{(v')^2} + \overline{(w')^2} \right) \tag{2.5}$$

where the turbulent velocity component is the difference between the instantaneous and average velocity $u' = u - \bar{u}$, whose mean and variance are

$$\overline{u'} = \frac{1}{T} \int_0^T \left(u(t) - \bar{u} \right) dt = 0 \tag{2.6}$$

and

$$\overline{(u')} = \frac{1}{T} \int_0^T \left(u(t) - \bar{u} \right)^2 dt \geq 0 \tag{2.7}$$

respectively.

The specific turbulence dissipation, ω, is the rate at which turbulence kinetic energy is converted into thermal internal energy per unit volume and time.

The standard k-ω model is based on the Wilcox (1998) k-ω model, which incorporates modifications for low-Reynolds number effects, compressibility, and shear flow spreading. One of the weak points of the Wilcox model is the sensitivity of the solutions to values for k and ω outside the shear layer (free-stream sensitivity).

The standard k-ω model is an empirical model based on model transport equations for the turbulence kinetic energy (k) and the specific dissipation rate (ω). To improve the accuracy of the model for predicting free shear flows, production terms have been added to both the k and ω equations over time.

Transport Equation for the Standard k-ω Model   The turbulence kinetic energy, k, and the specific dissipation rate, ω, are obtained from the following transport equations, respectively:

$$\frac{\partial}{\partial t}(\rho k) + \frac{\partial}{\partial x_i}(\rho k u_i) = \frac{\partial}{\partial x_j}\left(\Gamma_k \frac{\partial k}{\partial x_j}\right) + G_k - Y_k + S_k \qquad (2.8)$$

and

$$\frac{\partial}{\partial t}(\rho \omega) + \frac{\partial}{\partial x_i}(\rho \omega u_i) = \frac{\partial}{\partial x_j}\left(\Gamma_\omega \frac{\partial k}{\partial x_j}\right) + G_\omega - Y_\omega + S_\omega \qquad (2.9)$$

In these equations, G_k represents the generation of turbulence kinetic energy due to mean velocity gradients. G_ω represents the generation of ω. Γ_k and Γ_ω represent the effective diffusivity of k and ω, respectively. Y_k and Y_ω represent the dissipation of k and ω due to turbulence. S_k and S_k are user-defined source terms.

Modelling the Effective Diffusivity   The effective diffusivities for the k-ω model are given by:

$$\begin{aligned} \Gamma_k &= \mu + \frac{\mu_t}{\sigma_k} \\ \Gamma_\omega &= \mu + \frac{\mu_t}{\sigma_\omega} \end{aligned} \qquad (2.10)$$

where σ_k and σ_ω are the turbulent Prandtl numbers for k and ω, respectively. The turbulent viscosity, μ_t, is computed by combining k and ω as follows:

$$\mu_t = \alpha^* \frac{\rho k}{\omega} \qquad (2.11)$$

Low-Reynolds Number Correction   The coefficient α^* damps the turbulent viscosity causing a low-Reynolds number correction. It is given by:

$$\alpha^* = \alpha_\infty^* \left(\frac{\alpha_0^* + Re_t/R_k}{1 + Re_t/R_k} \right) \tag{2.12}$$

where,

$$Re_t = \frac{\rho k}{\mu \omega} \tag{2.13}$$

and

$$R_k = 6$$
$$\alpha_0^* = \frac{\beta_i}{3} \tag{2.14}$$
$$\beta_i = 0.072$$

In the high-Reynolds number form of the k-ω model, $\alpha^* = \alpha_\infty^* = 1$.

Modelling the Turbulence Production of k   The term G_k represents the production of turbulence kinetic energy. From the exact equation for the transport of k, this term may be defined as:

$$G_k = -\rho \overline{u_i' u_j'} \frac{\partial u_j}{\partial x_i} \tag{2.15}$$

To evaluate G_k in a manner consistent with the Boussinesq hypothesis,

$$G_k = \mu_t S^2 \tag{2.16}$$

where S is the is the modulus of the mean rate-of-strain tensor, defined as

$$S \equiv \sqrt{2 S_{ij} S_{ij}} \tag{2.17}$$

and the strain rate tensor, S_{ij} is defined as

$$S_{ij} = \frac{1}{2} \left(\frac{\partial u_j}{\partial x_i} + \frac{\partial u_i}{\partial x_j} \right) \tag{2.18}$$

Modelling the Turbulence Production of ω   The production of ω is given by:

$$G_w = \alpha \frac{\omega}{k} G_k \tag{2.19}$$

where G_k is given by Equation (2.16).

The coefficient α is given by:

$$\alpha = \frac{\alpha_\infty}{\alpha^*} \left(\frac{\alpha_0 + Re_t/R_\omega}{1 + Re_t/R_\omega} \right) \tag{2.20}$$

where $R_\omega = 2.95$. α^* and Re_t are given by Equation (2.12) and Equation (2.13), respectively.

Modelling the Turbulence Dissipation of k   The dissipation of k is given by:

$$Y_k = \rho \beta^* f_{\beta^*} k \omega \tag{2.21}$$

where,

$$f_{\beta^*} = \begin{cases} 1, & \chi_k \leq 0 \\ \frac{1+680\chi_k^2}{1+400\chi_k^2} & \chi_k > 0 \end{cases} \tag{2.22}$$

where,

$$\chi_k \equiv \frac{1}{\omega^3} \frac{\partial k}{\partial x_j} \frac{\partial \omega}{\partial x_j} \tag{2.23}$$

and

$$\beta^* = \beta_i^* \left[1 + \varsigma^* F(M_t) \right] \tag{2.24}$$

where β_i^* is given by

$$\beta_i^* = \beta_\infty^* \left(\frac{4/15 + (Re_t/R_\beta)^4}{1 + (Re_t/R_\beta)^4} \right) \tag{2.25}$$

and

$$\begin{aligned} \varsigma^* &= 1.5 \\ R_\beta &= 8 \\ \beta_\infty^* &= 0.09 \end{aligned} \tag{2.26}$$

where Re_t is given by Equation (2.13).

Modelling the Turbulence Dissipation of ω   The dissipation of ω is given by:

$$Y_\omega = \rho \beta f_\beta \omega^2 \tag{2.27}$$

where,

$$f_\beta = \frac{1 + 70\chi_\omega}{1 + 80\chi_\omega} \tag{2.28}$$

and

$$\chi_\omega = \left| \frac{\Omega_{ij}\Omega_{jk}S_{ki}}{(\beta_0^* \omega)^3} \right|$$
$$\Omega_{ij} = \frac{1}{2}\left(\frac{\partial u_i}{\partial x_j} - \frac{\partial u_j}{\partial x_i} \right) \tag{2.29}$$

The strain rate tensor, S_{ij} is defined as Equation (2.18). Also,

$$\beta = \beta_i \left[1 - \frac{\beta_i^*}{\beta_i} \varsigma^* F(M_t) \right] \tag{2.30}$$

where β_i^* is defined by Equation (2.25) and the compressibility function, $F(M_t)$, is given by:

$$F(M_t) = \begin{cases} 0, & M_t \leq M_{t0} \\ M_t^2 - M_{t0}^2 & M_t > M_{t0} \end{cases} \tag{2.31}$$

and,

$$M_t^2 \equiv \frac{2k}{a^2}$$
$$M_{t0} = 0.25 \tag{2.32}$$
$$a = \sqrt{\gamma RT}$$

In the high-Reynolds number form of the k-ω model, $\beta_i^* = \beta_i^* nfty$. In the incompressible form, $\beta^* = \beta_i^*$.

Model constants are as follows:
$\alpha_\infty^* = 1, \alpha_\infty = 0.52, \alpha_0 = \frac{1}{9}, \beta_\infty^* = 0.072, R_\beta = 8, R_k = 6, R_\omega = 2.95, \varsigma^* = 1.5, M_{t0} = 0.25, \sigma_k = 2.0, \sigma_\omega = 2.0$

Baseline (BSL) k-ω Model

The main problem with the Wilcox model is its well known strong sensitivity to free-stream conditions. The baseline (BSL) k-ω model was

developed to effectively blend the robust and accurate formulation of the k-ω model in the near-wall region with the free-stream independence of the k-ε model in the far-field. Hence, the k-ε model is converted into a k-ω formulation. The BSL k-ω model is similar to the standard k-ω model, but includes the following refinements:

- The standard k-ω model and the transformed k-ω model are both multiplied by a blending function, and both models are added together. The blending function is designed to be one in the near-wall region, which activates the standard k-ω model, and zero away from the surface, which activates the transformed k-ε model.

- The BSL model incorporates a damped cross-diffusion derivative term in the equation.

- The modeling constants are different.

Transport Equation for the BSL k-ω Model   The BSL k-ω model has a similar form to the standard k-ω model:

$$\frac{\partial}{\partial t}(\rho k) + \frac{\partial}{\partial x_i}(\rho k u_i) = \frac{\partial}{\partial x_j}\left(\Gamma_k \frac{\partial k}{\partial x_j}\right) + G_k - Y_k + S_k \qquad (2.33)$$

and

$$\frac{\partial}{\partial t}(\rho \omega) + \frac{\partial}{\partial x_i}(\rho \omega u_i) = \frac{\partial}{\partial x_j}\left(\Gamma_\omega \frac{\partial k}{\partial x_j}\right) + G_\omega - Y_\omega + S_\omega \qquad (2.34)$$

In these equations, all the terms are defined in the same manner as in the standard k-ω model.

Modelling the Effective Diffusivity   The effective diffusivities for the k-ω model are given by:

$$\begin{aligned}\Gamma_k &= \mu + \frac{\mu_t}{\sigma_k}\\[2mm]\Gamma_\omega &= \mu + \frac{\mu_t}{\sigma_\omega}\end{aligned} \qquad (2.35)$$

where σ_k and σ_ω are the turbulent Prandtl numbers for k and ω, respectively. The turbulent viscosity, μ_t, is computed as defined in Equation (2.11), and

$$\begin{aligned}\sigma_k &= \frac{1}{F_1/\sigma_{k,1} + (1 - F_1)/\sigma_{k,2}}\\[2mm]\sigma_\omega &= \frac{1}{F_1/\sigma_{\omega,1} + (1 - F_1)/\sigma_{\omega,2}}\end{aligned} \qquad (2.36)$$

The blending function F_1 is given by

$$F_1 = \tanh\left(\phi_1^4\right) \tag{2.37}$$

and

$$\phi_1 = \min\left[max\left(\frac{\sqrt{k}}{0.09\omega y}, \frac{500\mu}{\rho y^2 \omega}\right), \frac{4\rho k}{\sigma_{\omega,2}D_\omega^+ y^2}\right]$$
$$D_\omega^+ = max\left[2\rho\frac{1}{\sigma_{\omega,2}}\frac{1}{\omega}\frac{\partial k}{\partial x_j}\frac{\partial \omega}{\partial x_j}, 10^{-10}\right] \tag{2.38}$$

where y is the distance to the next surface and D_ω^+ is the positive portion of the cross-diffusion term (Equation (2.45)).

Modelling Turbulence Production of k   The term G_k represents the production of turbulence kinetic energy and is defined in the same manner as in the standard k-ω model.

Modelling Turbulence Production of ω   The term G_ω represents the production of ω and is given by

$$G_\omega = \frac{\alpha\alpha^*}{\nu_t}G_k \tag{2.39}$$

This formulation differs from the standard k-ω model (important for the SST model described in subsection (2.2.1)). It also differs from the standard k-ω model in the way the term α_∞ is evaluated. In the standard k-ω model, α_∞ is defined as a constant (0.52). For BSL k-ω model, α_∞ is given by

$$\alpha_\infty = F_1\alpha_{\infty,1} + (1-F_1)\alpha_{\infty,2} \tag{2.40}$$

where

$$\alpha_{\infty,1} = \frac{\beta_{i,1}}{\beta_\infty^*} - \frac{\kappa^2}{\sigma_{\omega,1}\sqrt{\beta_\infty^*}}$$
$$\alpha_{\infty,2} = \frac{\beta_{i,2}}{\beta_\infty^*} - \frac{\kappa^2}{\sigma_{\omega,2}\sqrt{\beta_\infty^*}} \tag{2.41}$$

where κ is 0.41.

Modelling the Turbulent Dissipation of k   The term Y_k represents the dissipation of turbulence kinetic energy and is defined similarly as in the standard k-ω model. The difference is in the way the term $f_{\beta*}$ is evaluated. In the standard k-ω model, $f_{\beta*}$ is defined as a piecewise function (Equation (2.22)). For the BSL k-ω model, $f_{\beta*}$ is a constant equal to 1. Thus,

$$Y_k = \rho \beta^* k \omega \tag{2.42}$$

Modelling the Turbulent Dissipation of ω   The term Y_ω represents the dissipation of ω and is defined in a similar manner as in the standard k-ω model. The difference is in the way the terms β_i and f_β are evaluated. In the standard k-ω model, β_i is defined as a constant (0.072) and f_β is defined in Equation (2.28). For BSL k-ω model, f_β is a constant equal to 1. Thus,

$$Y_k = \rho \beta \omega^2 \tag{2.43}$$

Instead of having a constant value, β_i is given by

$$\beta_i = F_1 \beta_{i,1} + (1 - F_1) \beta_{i,2} \tag{2.44}$$

and F_1 is obtained from Equation (2.37).

Cross-Diffusion Modification   The BSL k-ω model is based on both the standard k-ω model and the standard k-ε model. To blend these two models together, the standard k-ε model has been transformed into equations based on k and ω, which leads to the introduction of a cross-diffusion term D_ω. D_ω is defined as

$$D_\omega = 2(1 - F_1) \rho \frac{1}{\omega \sigma_{\omega,2}} \frac{\partial k}{\partial x_j} \frac{\partial \omega}{\partial x_j} \tag{2.45}$$

Model constants are as follows
$\sigma_{k,1} = 2.0, \sigma_{\omega,1} = 2.0, \sigma_{k,2} = 1.0, \sigma_{\omega,2} = 1.168, \beta_{i,1} = 0.075, \beta_{i,2} = 0.0828$

Shear-Stress Transport (SST) k-ω Model

The SST k-ω model includes not only all the refinements of the BSL k-ω model but also the transport of the turbulence shear stress in the definition of the turbulent viscosity. These features make the SST k-ω model more accurate and reliable for a broader class of flows than the standard and the BSL k-ω models.

Modelling the Turbulent Viscosity   The BSL model described previously combines the advantages of the Wilcox and the k-ε model, but still fails to properly predict the onset and amount of flow separation from smooth surfaces. The main reason is that both models do not account for the transport of the turbulent shear stress. This results in an over-prediction of the eddy-viscosity. The proper transport behaviour can be obtained by a limiter to the formulation of the eddy-viscosity:

$$\mu_t = \frac{\rho k}{\omega} \frac{1}{max\left[\frac{1}{\alpha^*}, \frac{SF_2}{\alpha_1 \omega}\right]} \tag{2.46}$$

where S is the strain rate magnitude and α^* is defined in Equation (2.12). The blending function F_1 is defined as Equation (2.37) and F_2 is given by

$$F_2 = \tanh\left(\phi_2^2\right) \tag{2.47}$$

$$\phi_2 = max\left[2\frac{\sqrt{k}}{0.09\omega y}, \frac{500\mu}{\rho y^2 \omega}\right] \tag{2.48}$$

where y is the distance to the next surface and D_ω^+ is the positive portion of the cross-diffusion term.

Model constants are as follows; $\sigma_{k,1} = 1.176, \sigma_{\omega,1} = 2.0, \sigma_{k,2} = 1.0, \sigma_{\omega,2} = 1.168, a_1 = 0.31, \beta_{i,1} = 0.075, \beta_{i,2} = 0.0828$. All additional model constants ($\alpha_\infty^*, \alpha_\infty, \alpha_0, \beta_\infty^*, R_\beta, R_k, R_\omega, \varsigma^*$, and M_{t0}) have the same values as for the standard k-ω model.

Turbulence Damping

In free surface flows, a high velocity gradient at the interface between two fluids results in high turbulence generation, in both phases. Hence, turbulence damping is required in the interfacial area to model such flows correctly. Egorov (2004) proposed the following term to be added as a source to the ω-equation

$$S_i = A_i \Delta n \beta \rho_i \left(\frac{B6\mu_i}{\beta \rho_i \Delta n^2}\right)^2 \tag{2.49}$$

where
A_i=Interfacial area density for phase i

Δn=Cell height normal to interface
β=0.075, k-ω model closure coefficient of destruction term
B=Damping factor
μ_i=Viscosity of phase i
ρ_i=Density of phase i

The interfacial area density for phase i is calculated as

$$A_i = 2.0\alpha_i|\nabla\alpha_i| \qquad (2.50)$$

where
α_i=Volume fraction of phase i
$|\nabla\alpha_i|$=Magnitude of gradient of volume fraction

The grid size Δn is calculated internally using grid information.

Wall Boundary Conditions

The wall boundary conditions for the k equation in the k-ω models are treated in the same way as the k equation is treated when enhanced wall treatments are used with the k-ε models which means that all boundary conditions for wall-function meshes will correspond to the wall function approach, while for the fine meshes, the appropriate low-Reynolds number boundary conditions will be applied.

The value of ω at the wall is specified as

$$\omega_W = \frac{\rho(u^*)^2}{\mu}\omega^+ \qquad (2.51)$$

Analytical solutions can be given for both the laminar sublayer

$$\omega^+ = \frac{6}{\beta_i(y^+)^2} \qquad (2.52)$$

and the logarithmic region:

$$\omega^+ = \frac{1}{\sqrt{\beta_\infty^*}}\frac{du_{turb}^+}{dy} \qquad (2.53)$$

Therefore, a wall treatment can be defined for the ω-equation, which switches automatically from the viscous sublayer formulation to the wall function, depending on the grid.

2.3   Volume of Fluid Method

2.3.1   Overview of the VOF Model

The VOF model can model two or more immiscible fluids by solving a single set of momentum equations and tracking the volume fraction of each of the fluids throughout the domain.

The VOF formulation relies on the fact that two or more fluids (or phases) are not inter-penetrating. For each additional phase added to the model, a variable is introduced: the volume fraction of the phase in the computational cell. In each control volume, the volume fractions of all phases sum to unity. The phases share the fields for all variables and properties that represent volume-averaged values as long as the volume fraction of each of the phases is known at each location. Thus the variables and properties in any given cell are either purely representative of one of the phases, or representative of a mixture of the phases, depending upon the volume fraction values. In other words, if the qth fluid's volume fraction in the cell is denoted as α_q, then the following three conditions are possible:

- $\alpha_q = 0$: The cell is empty (of the qth fluid).

- $\alpha_q = 1$: The cell is full (of the qth fluid).

- $0 < \alpha_q < 1$: The cell contains the interface between the qth fluid and one or more other fluids.

Based on the local value of α_q, the appropriate properties and variables will be assigned to each control volume within the domain.

2.3.2   Volume Fraction Equation

The tracking of the interface(s) between the phases is accomplished by the solution of a continuity equation for the volume fraction of one (or more) of the phases. For the phase, this equation has the following form:

$$\frac{1}{\rho_q} \left[\frac{\partial}{\partial t} \left(\alpha_q \rho_q \right) + \nabla \cdot \left(\alpha_q \rho_q \vec{v}_q \right) = S_{\alpha_q} + \sum_{p=1}^{n} \left(\dot{m}_{pq} \dot{m}_{qp} \right) \right] \qquad (2.54)$$

where $\dot{m}_{qp}$ is the mass transfer from phase q to phase p and $\dot{m}_{pq}$ is the mass transfer from phase p to phase q.

The volume fraction equation will not be solved for the primary phase; the primary-phase volume fraction will be computed based on the following constraint:

$$\sum_{q=1}^{n} \alpha_q = 1 \qquad\qquad (2.55)$$

The volume fraction equation may be solved either through implicit or explicit time formulation.

2.3.3   The Explicit Formulation

The explicit formulation is time-dependent and the volume fraction is discretized in the following manner:

$$\frac{\alpha_q^{n+1}\rho_q^{n+1} - \alpha_q^{n}\rho_q^{n}}{\Delta t}V + \sum_f \left(\rho_q U_f^{n}\alpha_{q,f}^{n}\right) = \left[S_{\alpha_q} + \sum_{p=1}^{n}\left(\dot{m}_{pq}\dot{m}_{qp}\right)\right]V$$

$$(2.56)$$

where:
$n+1$ = index for new (current) time step
n = index for previous time step
$\alpha_{q,f}$ = face value of the volume fraction
V = volume of cell
U_f = volume flux through the face, based on normal velocity

Since the volume fraction at the current time step is directly calculated based on known quantities at the previous time step, the explicit formulation does not require an iterative solution of the transport equation during each time step.

The face fluxes can be interpolated using interface tracking or capturing schemes such as Geo-Reconstruct, CICSAM, Compressive, and Modified HRIC.

When the explicit scheme is used, a time-dependent solution must be computed.

Interpolation Near the Interface

The geometric reconstruction and donor-acceptor schemes apply a special interpolation treatment to the cells that lie near the interface between

two phases. Figure (2.1) shows an actual interface shape along with the interfaces assumed during computation by these two methods.

(a) actual interface shape   (b) geo-reconstruct scheme   (c) donor-acceptor scheme
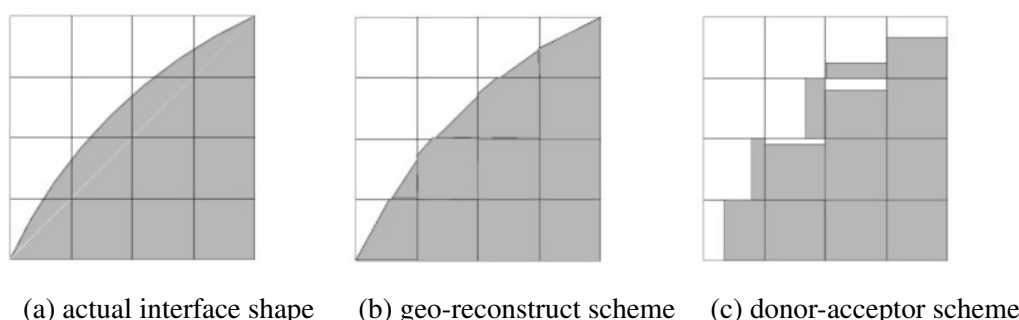
Figure (2.1)   Interface Calculations

The explicit scheme and the implicit scheme treat these cells with the same interpolation as the cells that are filled with one phase or the other which means using the standard upwind, second-order, QUICK, modified HRIC, compressive, or CICSAM scheme rather than applying a particular treatment.

In this chapter, the Geo-Reconstruct scheme is explained. More information on other schemes can be found in the Appendix B.

The Geometric Reconstruction Scheme   In the geometric reconstruction approach, the standard interpolation schemes are used to obtain the face fluxes whenever a cell is filled with one phase or another. When the cell is near the interface between two phases, the geometric reconstruction scheme is used.

The geometric reconstruction scheme represents the interface between fluids using a piecewise-linear approach. This scheme is the most accurate and is applicable for general unstructured meshes. It assumes that the interface between two fluids has a linear slope within each cell, and uses this linear shape for calculation of the advection of fluid through the cell faces.

The first step in this reconstruction scheme is calculating the position of the linear interface relative to the center of each partially-filled cell, based on information about the volume fraction and its derivatives in the cell. The second step is calculating the advecting amount of fluid through each face using the computed linear interface representation and information about the normal and tangential velocity distribution on the face. The third step is calculating the volume fraction in each cell using the balance of fluxes calculated during the previous step.

When the geometric reconstruction scheme is used, a time-dependent solution must be computed.

2.3.4   Momentum Equation

A single momentum equation is solved throughout the domain, and the resulting velocity field is shared among the phases. The momentum equation, shown below, is dependent on the volume fractions of all phases through the properties ρ and μ.

$$\frac{\partial}{\partial t}\left(\rho\vec{v}\right)+\nabla.\left(\rho\vec{v}\vec{v}\right)=-\nabla p+\nabla.\left[\mu\left(\nabla\vec{v}+\vec{v}^{T}\right)\right]+\rho\vec{g}+\vec{F} \qquad (2.57)$$

One limitation of the shared-fields approximation is that in cases where large velocity differences exist between the phases, the accuracy of the velocities computed near the interface can be adversely affected.

2.3.5   Material Properties

The properties appearing in the transport equations are determined by the presence of the component phases in each control volume. In a two-phase system, for example, if the phases are represented by the subscripts 1 and 2, and if the volume fraction of the second of these is being tracked, the density in each cell is given by

$$\rho = \alpha_2\rho_2 + \left(1-\alpha_2\right)\rho_1 \qquad (2.58)$$

In general, for a q-phase system, the volume-fraction-averaged density takes on the following form:

$$\rho = \sum\alpha_q\rho_q \qquad (2.59)$$

All other properties (for example, viscosity) are computed in this manner.

2.3.6   Additional Scalar Equations

Depending upon the problem definition, additional scalar equations may be involved in the solution. In the case of turbulence quantities, a single set of transport equations is solved, and the phases share the turbulence variables (for example, k and ω or the Reynolds stresses) throughout the field.

2.3.7   Surface Tension

The VOF model can also include the effects of surface tension along with the interface between each pair of phases. Surface tension arises as a result of attractive forces between molecules in a fluid. The surface tension is a force, acting only at the surface, that is required to maintain equilibrium in such instances. It acts to balance the radially inward inter-molecular attractive force with the radially outward pressure gradient force across the surface. In regions where two fluids are separated, but one of them is not in the form of spherical bubbles, the surface tension acts to minimize free energy by decreasing the area of the interface.

The calculation of surface tension effects on triangular and tetrahedral meshes is not as accurate as on quadrilateral and hexahedral meshes. The region where surface tension effects are most significant should, therefore, be meshed with quadrilaterals or hexahedrals.

In ANSYS Fluent, two surface tension models exist; the continuum surface force (CSF) and the continuum surface stress (CSS). The two models are described in detail in the following sections.

Continuum Surface Force Model

The continuum surface force (CSF) model has been implemented, such that the addition of surface tension to the VOF calculation results in a source term in the momentum equation. To understand the origin of the source term, consider the special case where the surface tension is constant along the surface, and where only the forces normal to the interface are considered. It can be shown that the pressure drop across the surface depends upon the surface tension coefficient, σ, and the surface curvature as measured by two radii in orthogonal directions, R_1 and R_2:

$$p_2 - p_1 = \sigma \left(\frac{1}{R_1} + \frac{1}{R_2} \right) \tag{2.60}$$

where p_1 and p_2 are the pressures in the two fluids on either side of the interface.

In the CSF model, the surface curvature is computed from local gradients in the surface normal at the interface. Let n be the surface normal, defined as the gradient of α_q, the volume fraction of the qth phase.

$$n = \nabla \alpha_q \tag{2.61}$$

The curvature, κ, is defined in terms of the divergence of the unit normal, $\hat{n}$,

$$\kappa = \nabla.\hat{n} \tag{2.62}$$

where,

$$\hat{n} = \frac{\vec{n}}{|\vec{n}|} \tag{2.63}$$

The surface tension can be written in terms of the pressure jump across the surface. The force at the surface can be expressed as a volume force using the divergence theorem. It is this volume force that is the source term that is added to the momentum equation. It has the following form:

$$F_{vol} = \sum_{pairs\, ij,i<j} \sigma_{ij} \frac{\alpha_i \rho_i \kappa_j \nabla \alpha_j + \alpha_j \rho_j \kappa_i \nabla \alpha_i}{\frac{1}{2}(\rho_i + \rho_j)} \tag{2.64}$$

This expression allows for a smooth superposition of forces near cells where more than two phases are present. If only two phases are present in a cell, then $\kappa_i = -\kappa_j$ and $\nabla \alpha_i = -\nabla \alpha_j$, and Equation (2.64) simplifies to:

$$F_{vol} = \sigma_{ij} \kappa_i \frac{\rho \nabla \alpha_i}{\left(\frac{\rho_i + \rho_j}{2}\right)} \tag{2.65}$$

where ρ is the volume-averaged density computed using Equation (2.59). Equation (2.65) shows that the surface tension source term for a cell is proportional to the average density in the cell.

Continuum Surface Stress Model

The Continuum Surface Stress (CSS) method is an alternative way to model surface tension conservatively, unlike the non-conservative formulation of the Continuum Surface Force (CSF) method. CSS avoids the explicit calculation of curvature and could be represented as an anisotropic variant of modeling capillary forces based on surface stresses.

In the CSS method, the surface stress tensor due to surface tension is represented as

$$T = \sigma(I - \hat{n} \otimes \hat{n})|\hat{n}| \tag{2.66}$$

and,

$$\vec{n} = \nabla \alpha \tag{2.67}$$

where, I = unit tensor

σ = surface tension coefficient

$\otimes$ = tensor product of the two vectors: the original normal and the transformed normal

α = volume fraction

$\vec{n}$ = volume fraction gradient

So,

$$T = \sigma \left(|\nabla\alpha|I - \frac{\nabla\alpha \otimes \nabla\alpha}{|\nabla\alpha|} \right) \tag{2.68}$$

The surface tension force is represented as

$$F_{CSS} = \nabla.T \tag{2.69}$$

Comparing the CSS and CSF Methods   The CSS method provides few added advantages over the CSF method, especially for cases involving variable surface tension. Both CSS and CSF methods introduce parasitic currents at the interface due to the imbalance of the pressure gradient and surface tension force.

In the CSF method, the surface tension force is represented in a non-conservative manner as follows:

$$F_{CSF} = \sigma\kappa\nabla\alpha \tag{2.70}$$

where κ is the curvature. This expression is valid only for constant surface tension.

For variable surface tension, the CSF formulation requires to model an additional term in the tangential direction to the interface based on the surface tension gradient.

In the CSS method, surface tension force is represented in a conservative manner as follows:

$$F_{CSS} = \nabla. \left[\sigma \left(|\nabla\alpha|I - \frac{\nabla\alpha \otimes \nabla\alpha}{|\nabla\alpha|} \right) \right] \tag{2.71}$$

The CSS method does not require any explicit calculation for the curvature. Therefore, It performs more physically in under-resolved regions, such as sharp corners. Furthermore, this method does not require any additional terms for modeling variable surface tension due to its conservative formulation.

Chapter 3

Experimental Benchmarking

The experimental data were collected at the facility in Multiphase Thermo-Fluid Dynamics Laboratory at Politecnico di Milano.

The schematic of the experimental loop is shown in Figure (3.1). A storage tank of 4 m^3 volume supplies the water flow employing a centrifugal pump, and the volume flow rate is measured by a float-type flow meter set through a valve. The characteristics of the centrifugal pump and the flow meters are shown in Table (3.1) and (3.2), respectively.
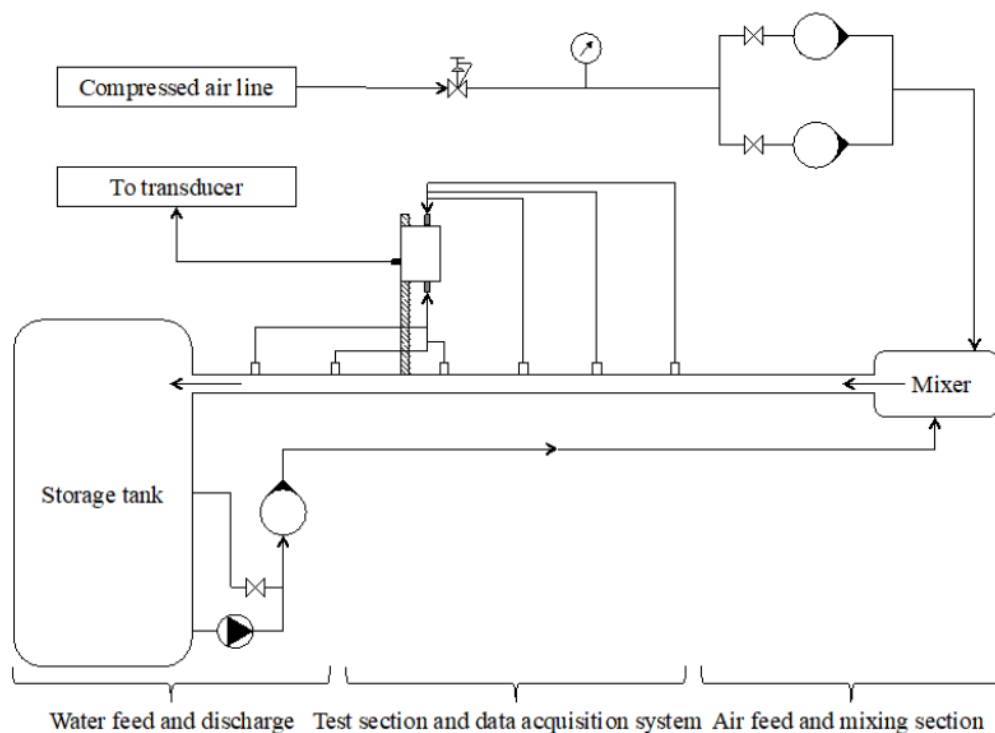
Figure (3.1)   Set-Up Loop Schematic

(b) Experimental Mixing Section
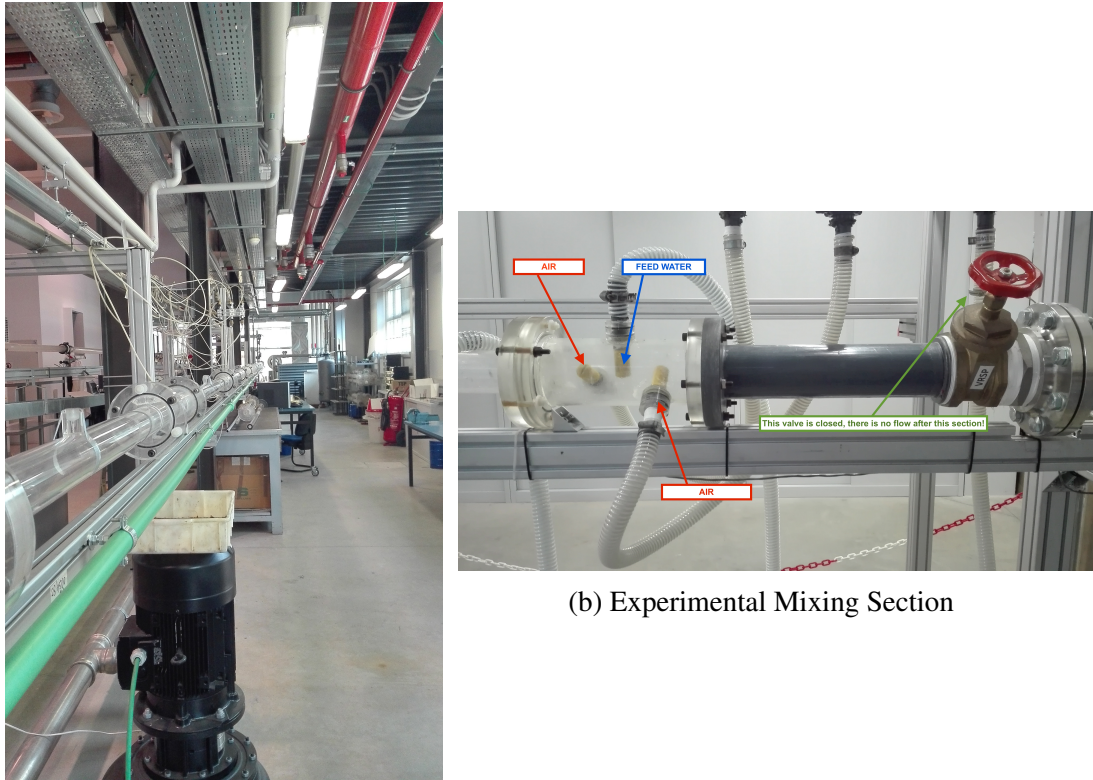
(a) Experimental Set-Up Loop

Figure (3.2)   Experiment Facility

Table (3.1)   Centrifugal Pump Characteristics

Name	CALPEDA
Volume Flow Rate Range	$0.12 - 0.75 \ m^3/h$
Head Range	6.5 - 20 m

Table (3.2)   Flow-meters Characteristics

Name	ASAMETRO P13-2800	ASAMETRO N5-2008
Fluid	Water	Air
Range	$0.1 - 1 \ m^3/h$	$2.5 - 23.5 \ Sm^3/h$
Error	$\pm 3\%$ full scale	$\pm 2.5\%$ full scale
T_{cal}	20 °C	20 °C
p_{cal}	-	101 325 Pa

Air and water mix in the mixing section where compressed air is injected into the liquid flow. After the air-water mixing section, the two-phase fluid flows inside the test section consisted of a 24m long horizontal PMMA pipeline of 60 mm bore tubes connected by sealed flanges.

There are four evenly distributed pressure taps along the pipeline that are connected to a differential pressure transducer. Each of the taps is placed at a distance of at least ten diameters from the flanges. The characteristics of the pressure transducer are shown in Table (3.3). The superficial velocities ranged between 0.03 m/s and 0.06 m/s for the water and between 0.41 m/s and 2.31 m/s for air. The experiments were conducted repeatedly to ensure the reliability of the achieved results. The pressure gradient along the pipeline was determined.

Table (3.3)   Pressure Transducer characteristics

Name	SETRA 267 MR 7
Output	$0 - 5$ V
Range	$0 - 250 / 0 - 1\,000$ Pa
Fluid	Gas
Error	± 1 % full scale

Moreover, the height of the water layer is measured with a modified method developed by Kang and Kim [2]. This method consists of a needle electrode introduced radially from above through an open pressure tap with a ruler to measure the immersion depth and a reference electrode submerged through a second pressure tap into the liquid phase. The needle electrode is connected to an analogue input of the acquisition board and grounded through a resistance while the reference electrode is connected to a power supply. Figure (3.3) shows a schematic of the used method.
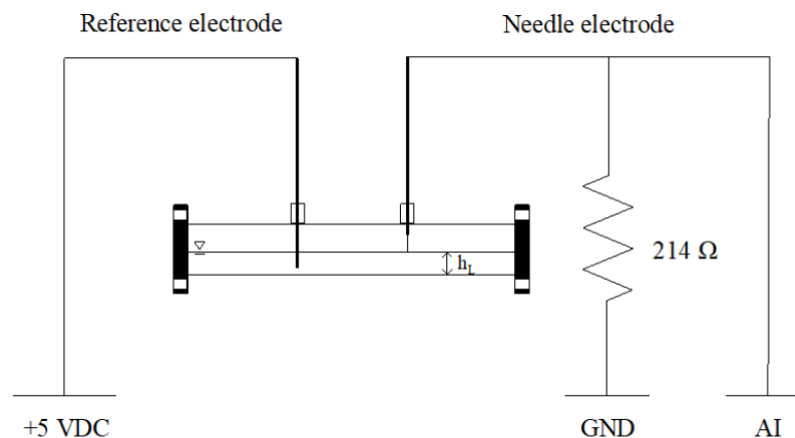
Figure (3.3)   Schematic of Water Level Measurement Technique

This way, the difference between the pipe inner diameter and the maximum water layer depth h_L can be measured. Accordingly, void fraction

values are obtained from Equations (3.1) and (3.2), where γ is the angle subtended by two radii to the ends of the interface perimeter S_i as shown in Figure (3.4).
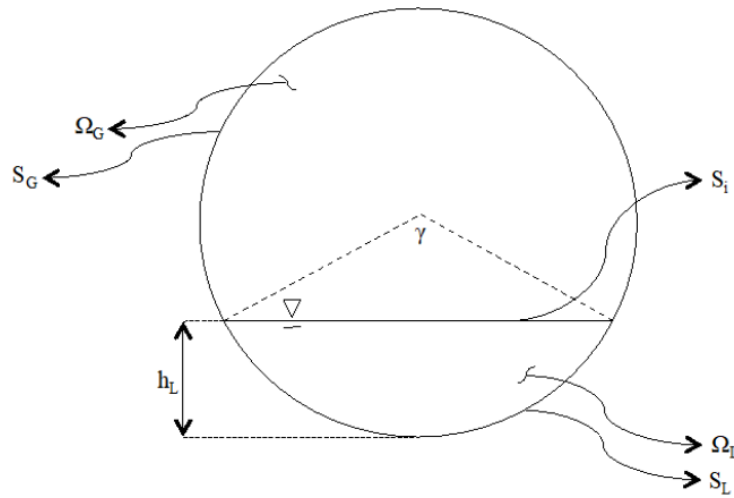

Figure (3.4)   Pipe Cross-Section

$$\gamma = 2\cos^{-1}\left(1 - \frac{2h_L}{D}\right) \tag{3.1}$$

$$\alpha = 1 - \frac{\gamma - \sin\gamma}{2\pi} \tag{3.2}$$

The experimental results are collected in Table (C.1) in the Appendix C. Furthermore, they are shown in Mandhane's map as shown in Figure (3.5).
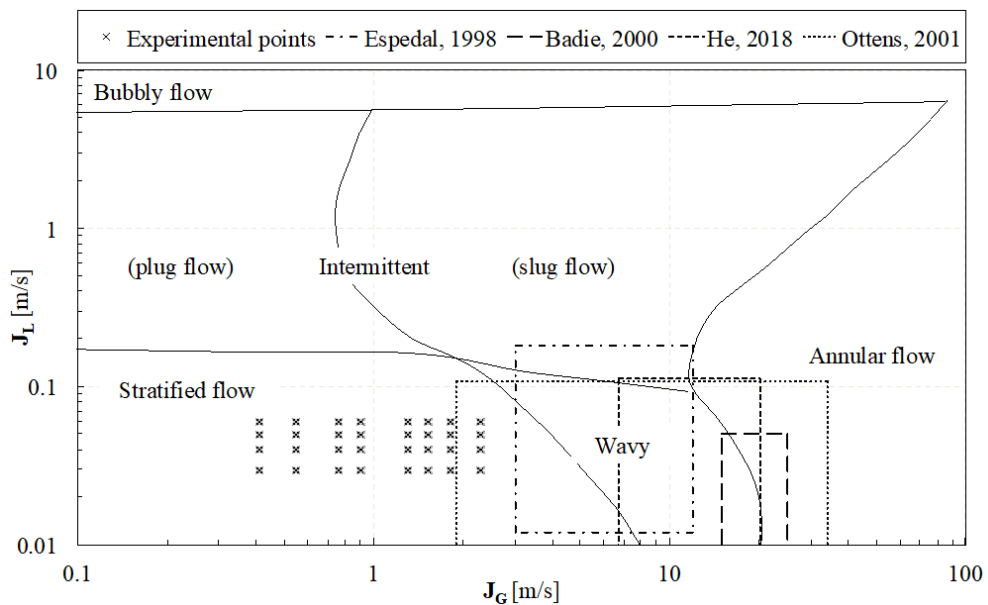

Figure (3.5)   Experimental Data on the Mandhane's Map

Chapter 4

Numerical Modelling in ANSYS

4.1 Geometry

The geometry of the studied case is shown in Figure (4.1). This geometry consists of a pipe with a bore diameter of 60 *mm* and a length of 2 *m*. A portion of the pipe used in experiments is simulated to capture the details of the interface by adopting a refined mesh. This approach is computationally unaffordable if a complete experimental model is simulated.

The geometry has been divided into two parts, where each corresponds to one of the phases. This division varies from case to case according to the void fraction.
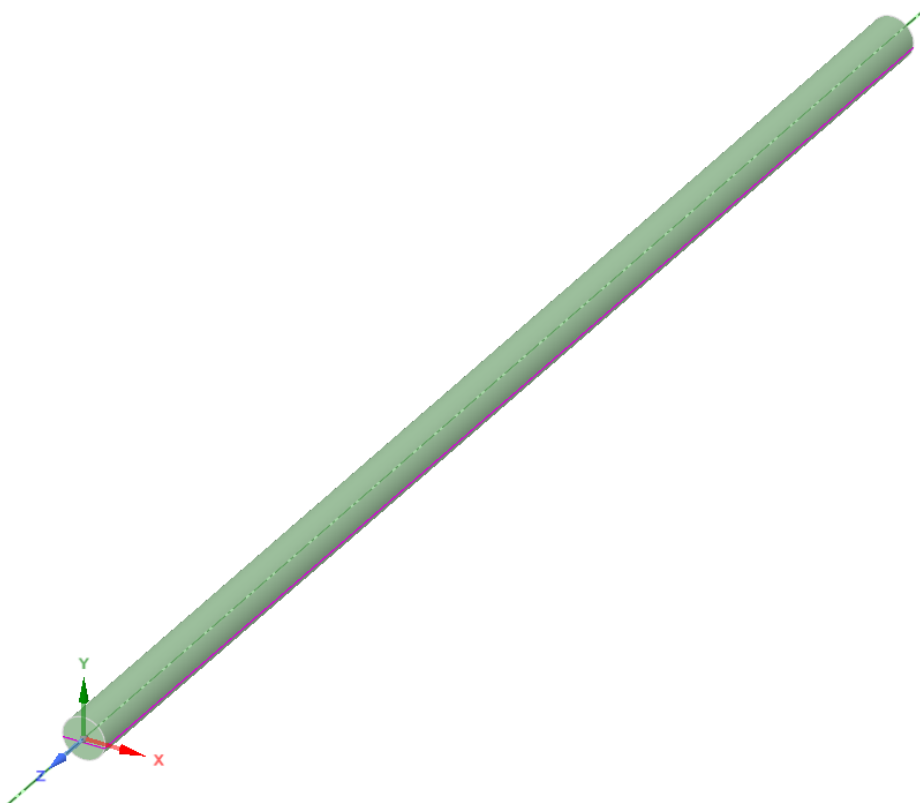
Figure (4.1)   Geometry of the Case

4.2   Mesh

Meshes are commonly used to compute solutions of partial differential equations. A mesh partitions space into elements (or cells or zones) over which the equations can be solved, which then approximates the solution over the larger domain.

In this section, the focus is on the cell shapes and grid characteristics of the generated mesh for the simulation. Thus, only these parts are described in detail.

4.2.1   Cell Shape

In the mesh generation, three-dimensional hexahedral elements are used. For the same cell amount, the accuracy of solutions in hexahedral meshes is the highest. The pyramid and triangular prism zones can be considered computationally as degenerate hexahedral elements, where some edges have been reduced to zero.

4.2.2   Grid Class

The generated mesh is composed of a structured grid. This type of grid is identified by regular connectivity. The possible element choices are quadrilateral in 2D and hexahedral elements in 3D. This model is highly space-efficient since a storage arrangement defines the neighborhood relationships. Structured grids have better convergence and higher resolution compared to unstructured ones.

Although the manual creation of a structured grid is more time consuming compared to the unstructured meshes, the unstructured grid needs more CPU time and memory.

4.2.3   Accuracy

Both discretization error and solution error have an impact on accuracy. For discretization error, a given mesh is a discrete approximation of the space, and so can only provide an approximate solution, even when equations are solved exactly. Furthermore, many iterations over the entire mesh are required for PDEs, and the calculation is terminated early before the equations are solved exactly.

Accuracy depends on the total number of elements and the shape of individual elements. The speed of each iteration grows (linearly) with

the number of elements, and the required number of iterations depends on the local solution value and gradient compared to the shape and size of local elements.

4.2.4   Generated Mesh

A mesh is considered to have higher quality if a more accurate solution is calculated more quickly. A poor-quality grid will cause inaccurate solutions and slow convergence. In order to have a good quality mesh, the following characteristics of the grid are considered:

- For the same cell count, hexahedral meshes are used to obtain more accurate solutions, especially in this case that the grid lines are aligned with the flow.

- The mesh density is high enough to capture all relevant flow features.

- The mesh adjacent to the wall is fine enough to resolve the boundary layer flow. Also, an inflated mesh refinement in the interface domain is applied to capture the behavior of the interface elaborately.

The final generated mesh is shown in Figure(4.2).
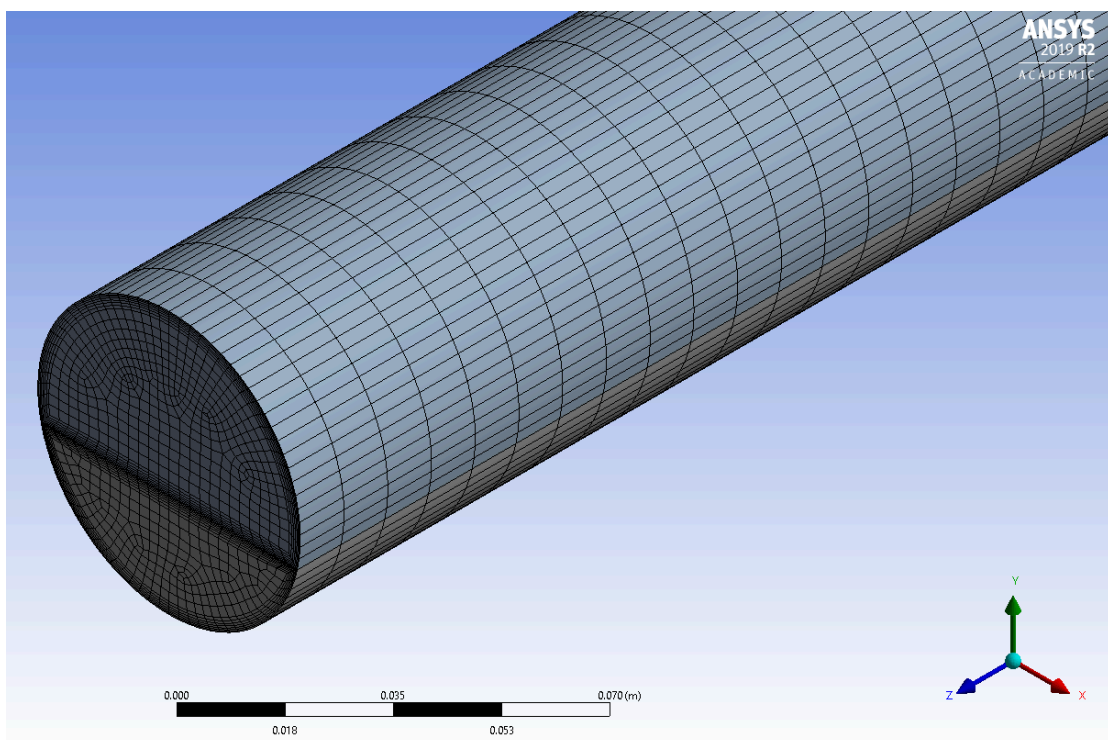
Figure (4.2)   Generated Mesh

Moreover, another mesh is generated with further refinement at the interface to investigate the effect of grid refinement at the interface on the pressure gradient and capture any waviness at the interface for both stratified and wavy regimes. This mesh is shown in Figure(4.3).
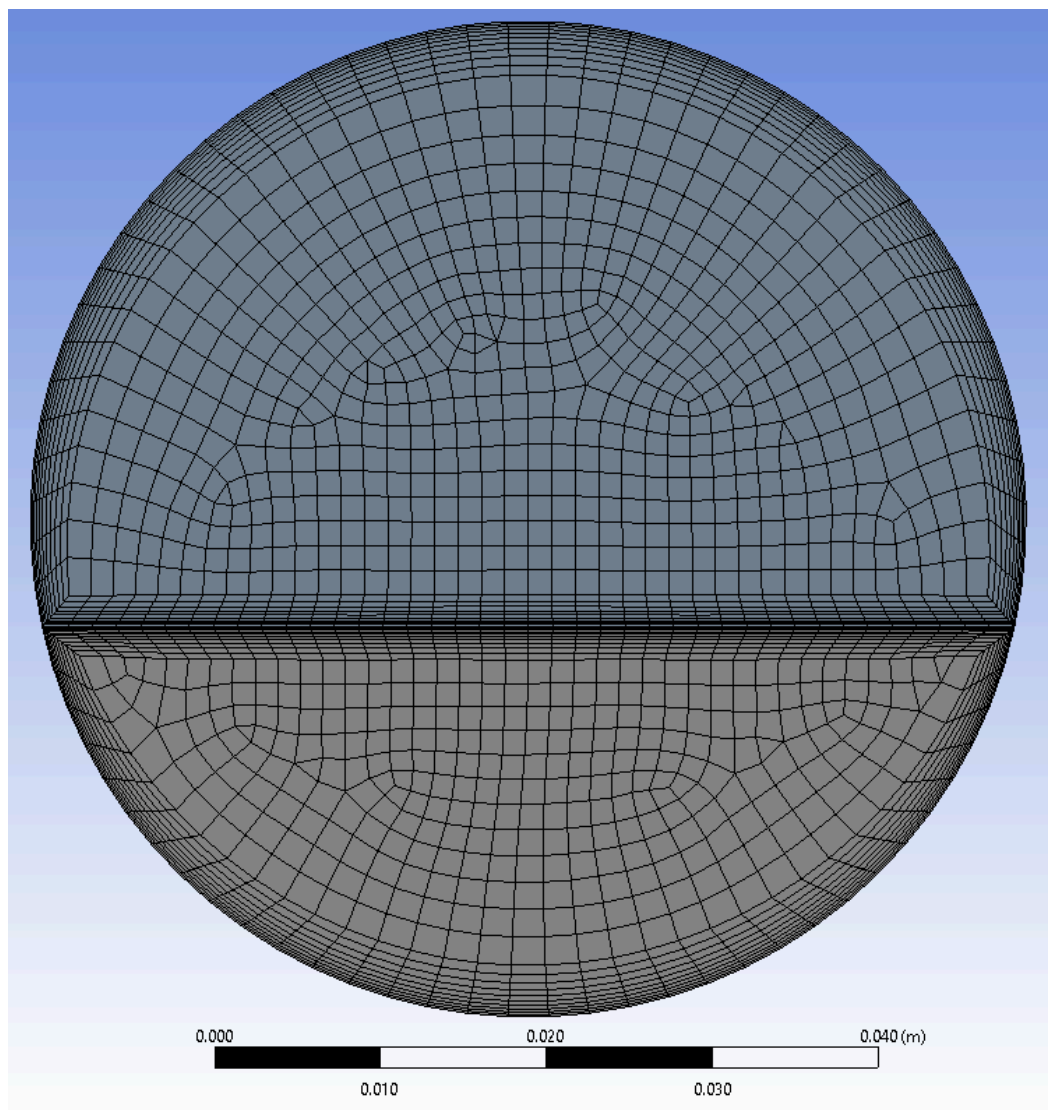

Figure (4.3)   Generated Mesh with Further Refinement at the Interface

4.2.5 Grid Independence

A solution is considered grid-independent if the discretization and solution errors are small enough given sufficient iterations, which is essential to consider for comparative results. A mesh convergence study consists of refining elements and comparing the refined solutions to coarse solutions. If further refinement (or other changes) does not significantly change the solution, the mesh is an "Independent Grid".

Mesh independence of the results is carried out for the case of Ex-

periment #10 (see Table(C.1)) with $J_l = 0.04[m/s]$, $J_g = 0.5513[m/s]$, $(dp/dz)_{experimental} = 0.486[Pa/m]$, and void fraction of 0.705. For this matter, three grids were generated with 169 349, 292 000, and 505 261 elements. The generated grids are shown in Figure(4.4).
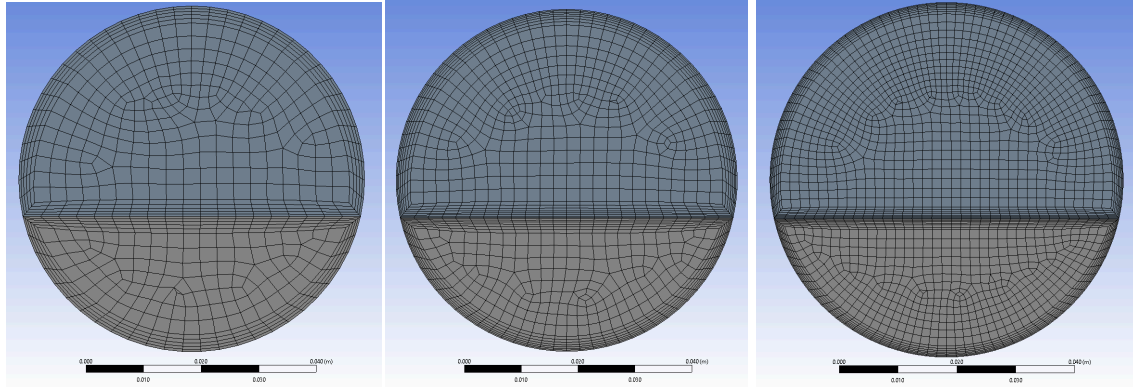
(a) 169 349 Elements Mesh   (b) 292 000 Elements Mesh   (c) 505 261 Elements Mesh

Figure (4.4)   Three Grids Generated for Mesh Independence Study

The results, Figure(4.5), show that the pressure drop of the 292 000 grid has 14.98% difference from the 169 349 grid; however, the pressure drop of the 505 261 grid has only 1.637% difference with 292 000 grid. Thus, it can be said that the independence of the grid has been reached.

Figure (4.5)   Mesh Independence of the Pressure Gradient

A non-dimensional wall distance for a wall-bounded flow can be defined in the following way:

$$y^+ \equiv \frac{u_* y}{\nu} \tag{4.1}$$

where u_* is the friction velocity at the nearest wall, y is the distance to the nearest wall and ν is the local kinematic viscosity of the fluid.

Figure (4.6), (4.7), and (4.8) show the y^+ histogram for different numbers of mesh elements. The most satisfactory results were obtained for 505 261 elements mesh. The maximum value of y^+ is observed at the line where the interface between air and gas meets the wall due to the very small size of the grid in this region. Moreover, there is a small difference between the three grids in the value of y^+ because of the small difference in the mesh size in the vicinity of the interface.
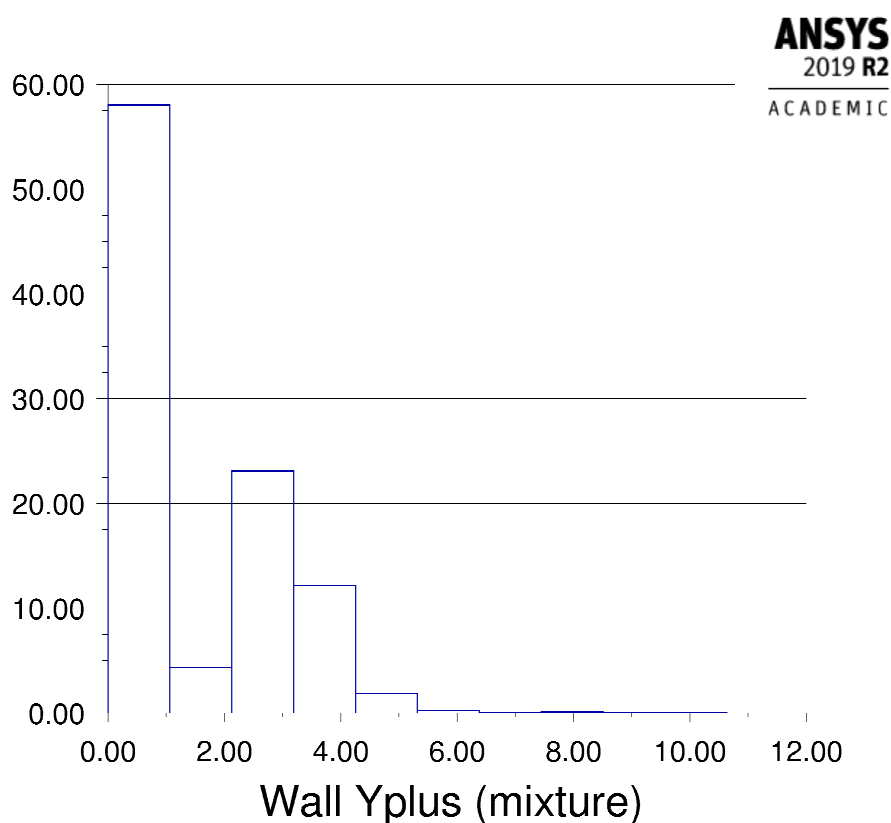
Figure (4.6)   Y Plus Histogram for 169 349 Mesh
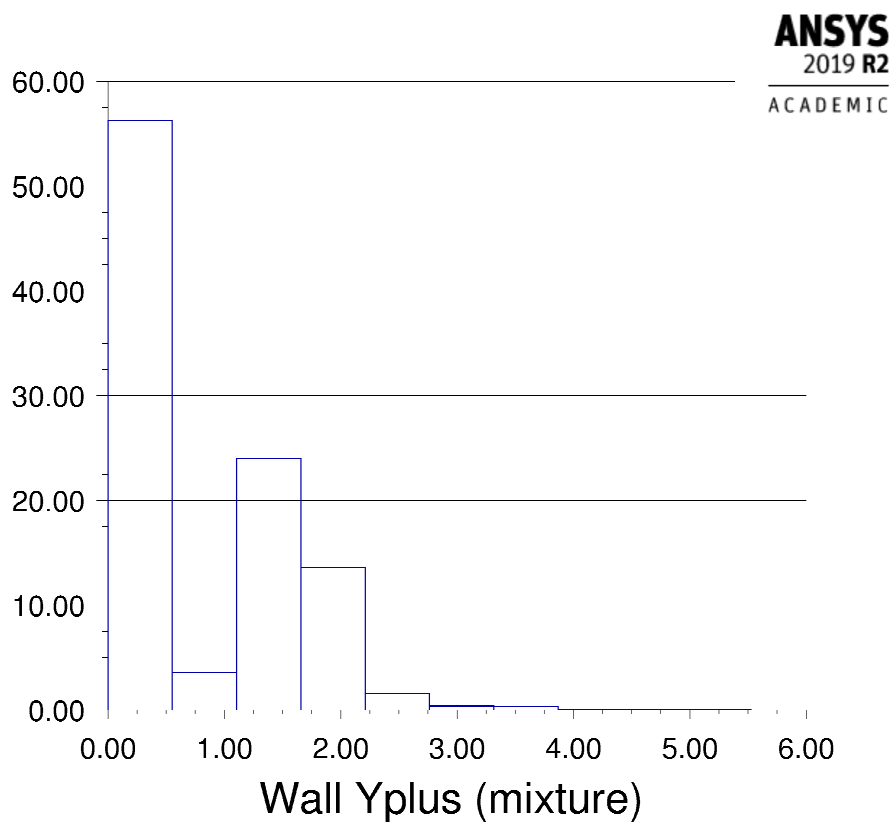
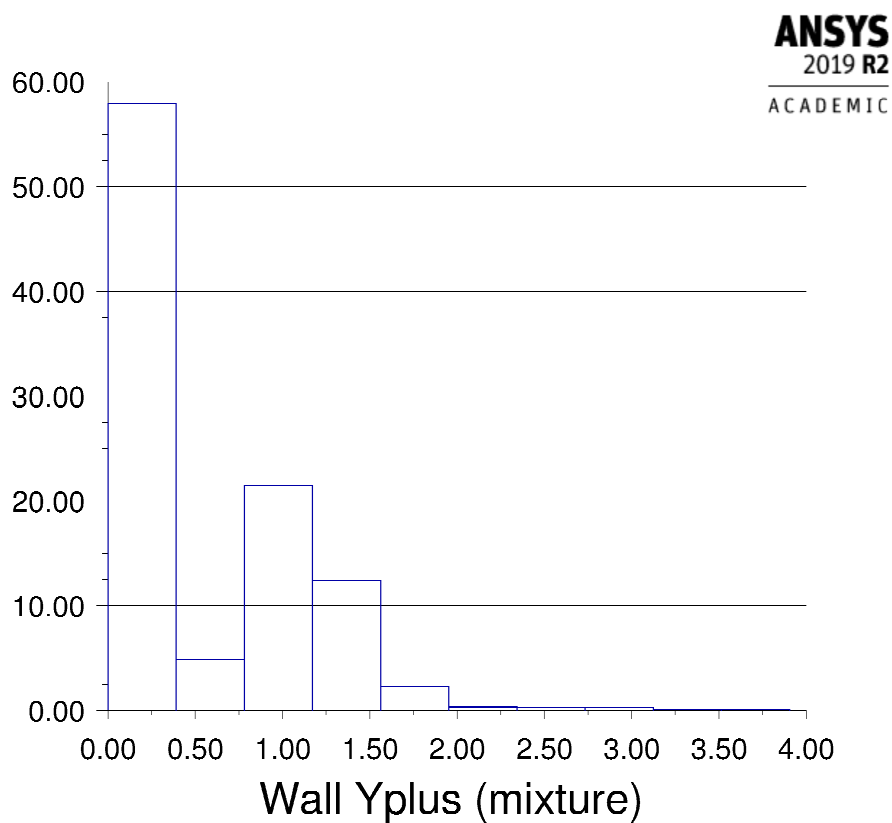Figure (4.7)   Y Plus Histogram for 292 000 Mesh

Figure (4.8)   Y Plus Histogram for 505 261 Mesh

4.3 Model Set-Up in ANSYS Fluent

4.3.1 Set-Up Procedure

The steps for setting up and solving a general multiphase problem is outlined below and described in detail for the case study in the subsection that follows.

1. Enabling the multiphase model (in this case, VOF) and specifying the number of phases is the first step. For the VOF model, the volume fraction scheme is also specified.

2. Enabling the viscous model by choosing the k-ω SST turbulence model is the second step. In this case, the turbulence damping is activated as well.

3. Selecting the material representing each phase from the materials database is the third step.

4. Defining the phases, and specifying any interaction between them (in this case, surface tension for using the VOF model) is the fourth step.

5. Enabling gravity and specifying the gravitational acceleration is the fifth step. This step is mandatory because of the presence of body forces.

6. Specifying the boundary conditions, including the secondary-phase volume fraction at flow boundaries is the sixth step.

7. Setting any model-specific solution parameters required for the case study is the seventh step.

8. Initializing the solution and setting the initial volume fractions for the secondary phase is the eighth step.

9. Calculating a solution and examining the results is the final step.

4.3.2 Final Model Set-Up

In this study, specifying the volume fraction formulation to be used for the VOF multiphase model is of great importance. ANSYS Fluent offers Implicit and Explicit formulation; however, Explicit schemes are time-dependent which is suitable for the studied case. Among all the options

for Volume Fraction spatial discretization schemes, Geo-Reconstruct is chosen.

Although the Geo-Reconstruct scheme is computationally expensive, the interface between phases will be sharper than the predicted with other schemes. The geometric reconstruction interpolation scheme is typically used whenever a time-accurate transient behavior of the VOF solution is being studied. In this case, the Explicit formulation of Volume Fraction Parameters is used with the Geo-Reconstruct scheme.

Since large body forces (in this case, gravity and surface tension forces) exist in the multiphase flow, the body force and pressure gradient terms in the momentum equation are almost in equilibrium while the contributions of convective and viscous terms are small in comparison. Unless partial equilibrium of pressure gradient and body forces is taken into account, segregated algorithms converge poorly. By enabling "Implicit Body Force" in ANSYS Fluent, a more robust solution is provided.

To include the body force, Gravity is enabled in the Operating Conditions, and the Gravitational Acceleration is specified as $-9.81[m/s^2]$ in the Y direction. For VOF calculations, the Specified Operating Density option is enabled as well in the Operating Conditions, and the Operating Density is set to be the density of the lightest phase, which is air.

The two Eulerian phases selected are water and air as primary and secondary, respectively. The material properties were already available in the ANSYS Fluent database; however, a sensitivity analysis on the density of air is conducted where the density of humid air is inserted instead of the density of dry air.

The Inlet Volume Fraction and Outlet Backflow Fraction have been set according to the void fraction of each specific case. Air and water enter the pipe from the upper and lower parts of the inlet, respectively.

The Second Order Upwind method is chosen for Spatial Discretization of Momentum, Turbulent Kinetic Energy, and Specific Dissipation Rate since high precision and accuracy is of great importance.

For the case of $J_l = 0.04[m/s]$, $J_g = 0.5513[m/s]$, $(dp/dz)_{experimental} = 0.486[Pa/m]$, and void fraction of 0.705, a Hybrid Initialization has been conducted followed by a patch to distinguish the two phases in the pipe. For all other cases, however, an interpolation of the results from the case as mentioned earlier at 20 seconds of flow-time, is used to initialize the simulation.

The summary of the simulation is shown in Table (4.1).

Table (4.1)   Summary of the Simulation in ANSYS Fluent

Solver	Pressure-based Type Absolute Velocity Formulation Transient
Gravitational Acceleration	$-9.81 m/s^2$ in Y Direction
Multiphase Model	Volume of the Fluid – Two Phases Explicit Formulation Implicit Body Force Sharp Interface Modelling Interfacial Anti-Diffusion
Viscous Model	k-ω SST Turbulence Damping (Damping Factor = 250)
Phase-Interaction	Surface Tension Force Modelling Continuum Surface Force Constant Surface Tension Coefficient = 0.073 N/m
Materials	Water-Liquid (Primary Phase) Air (Secondary Phase)
Operating Conditions	Atmospheric Pressure Gravity = $-9.81 m/s^2$ in Y Direction Density = 1.225 kg/m^3
Boundary Conditions	Inlet: Velocity Inlet - Inlet Volume Fraction Wall: Stationary – No Slip Condition Outlet: Pressure Outlet - Outlet Backflow Fraction
Solution Methods	Pressure-Velocity Coupling: SIMPLE Spatial Discretization of Pressure: PRESTO! Spatial Discretization of Volume Fraction: Geo-Reconstruct High Order Term Relaxation

Chapter 5

Results and Discussion

5.1 First Case Scenario - Stratified Smooth Flow

As Taitel and Duckler (1976) explained in their study, the Reynolds number should be calculated by using the actual velocity and hydraulic diameter of each phase to determine whether the laminar or turbulent flow occurs in each phase. According to the data from the experiments, this Reynolds number can be calculated for each phase. This Reynolds number range for the gas phase is from 2 844 to 15 867, while the for the liquid phase ranges from 4 183 to 8 366. So, the flow is entirely turbulent for both phases.

Defining the turn-over time as the time required for a single particle to travel from the inlet point to the outlet point, the solution is calculated for two turn-over times of the water phase. Since water has a lower velocity than air, the velocity of water is the criteria for data post-processing in this transient simulation.

The results are shown for Experiment #10 (see Table (C.1)). Other simulated cases have a similar set-up for which analogous results are achieved.

Figure (5.1) shows the water level and the interface between gas and liquid phases along the axis of the pipe. Figure (5.2) shows the interface at different cross-sections along the pipe axis. Both of these figures show that the stratified smooth flow is accomplished through the simulation as no waves of any amplitude or wavelength are observed. The interface is flat not only along the pipe axis but also at the cross-section.

Figure (5.3) represents the contours of velocity magnitude of both phases along the axis of the pipe. Figure (5.4) shows the velocity magnitude contours at the half-length cross-section of the pipe. Obviously, the velocity at the wall is zero due to the no-slip condition.
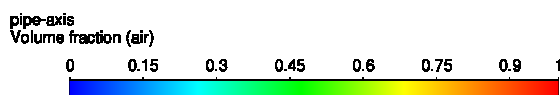
Figure (5.1)   Contours of the Phases at the Pipe Axis
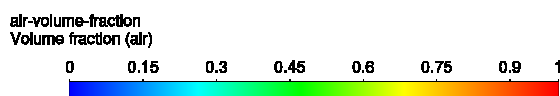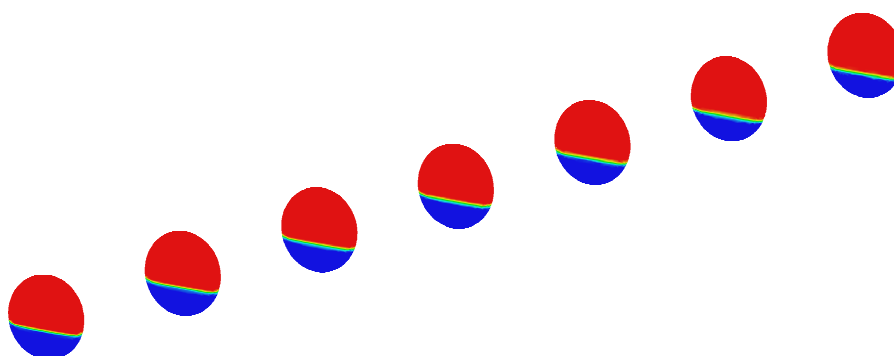

Figure (5.2)   Contours of the Phases at Multiple Cross-Sections Along the Pipe
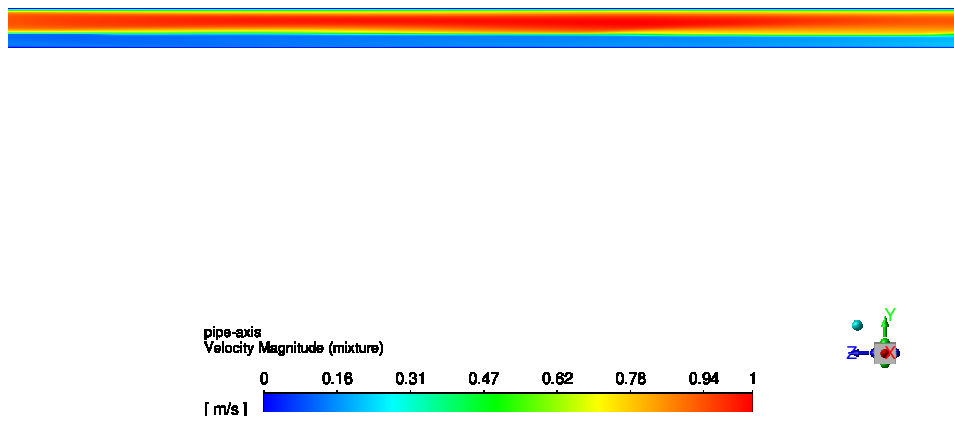
Figure (5.3)   Contours of the Velocity Magnitude at the Pipe Axis
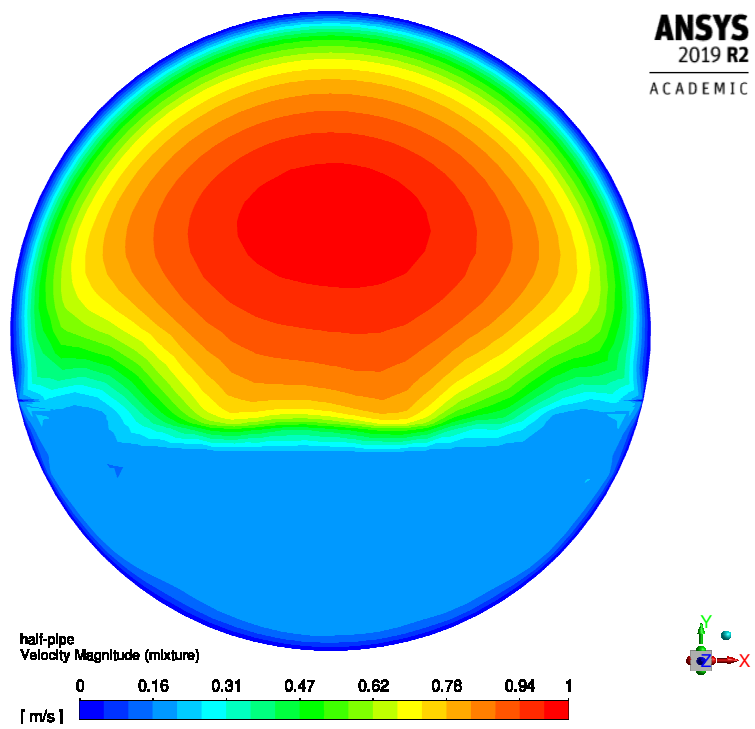

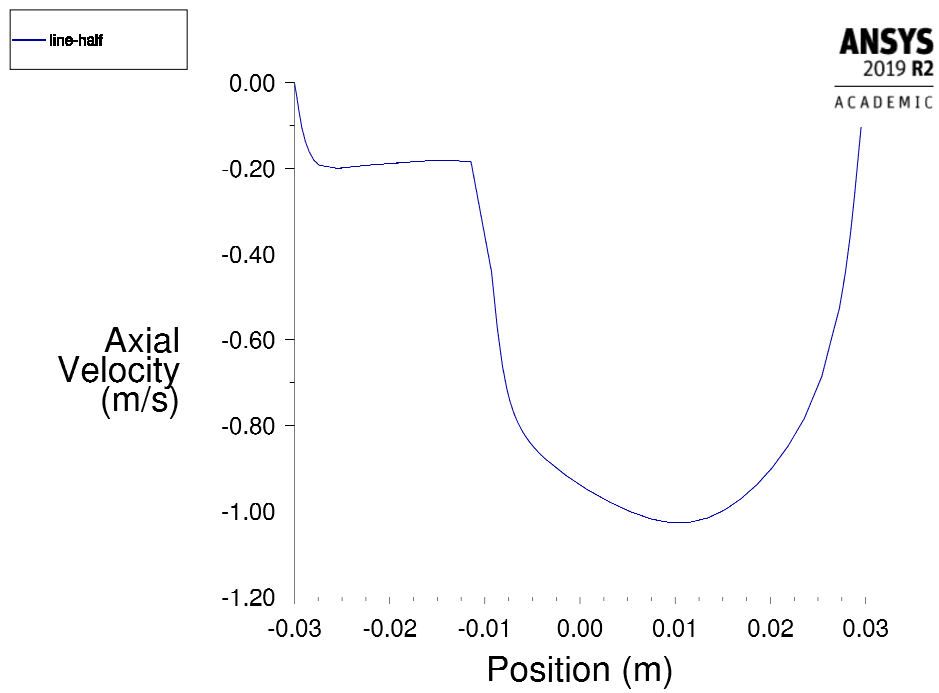Figure (5.4)   Contours of the Velocity Magnitude at the Half-Length Cross-Section

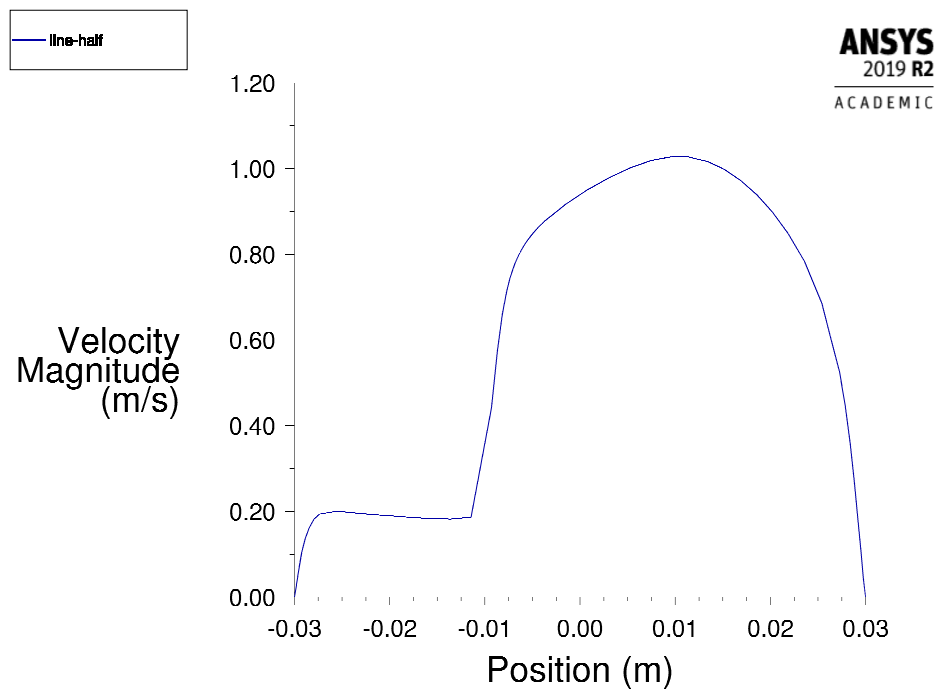Figure (5.5)   Axial Velocity Profile at the Half-Length Cross-Section

Figure (5.6)   Velocity Magnitude Profile at the Half-Length Cross-Section

Figure (5.7) and (5.8) show the contours of turbulence kinetic energy along the pipe axis and at the half-length cross-section of the pipe, respectively. As it is shown, the turbulence kinetic energy is higher in the gas phase, and it is higher, especially at the interface between gas and liquid phases. The turbulence kinetic energy is generated by the shear stress due to the eddies generated through the turbulent flow. The reason for the high kinetic energy is the generation of vortices in the air phase at the area close to the interface and the walls on both sides. These vortices have a very high velocity magnitude, which generates a very high kinetic energy, as shown in Figure (5.9). Some vortices can be observed in the water phase as well; however, the velocity magnitude of these vortices is not sufficiently high to have a significant effect on the turbulent kinetic energy.
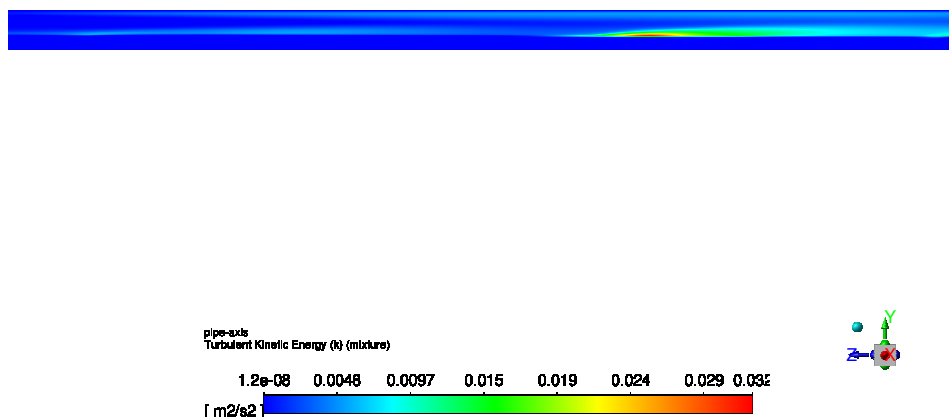

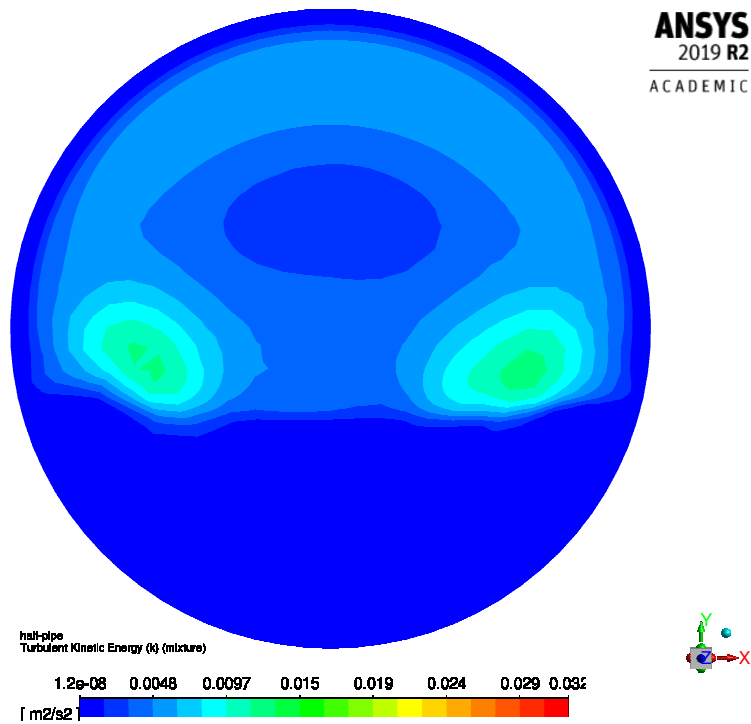Figure (5.7)   Contours of the Turbulence Kinetic Energy at the Pipe Axis

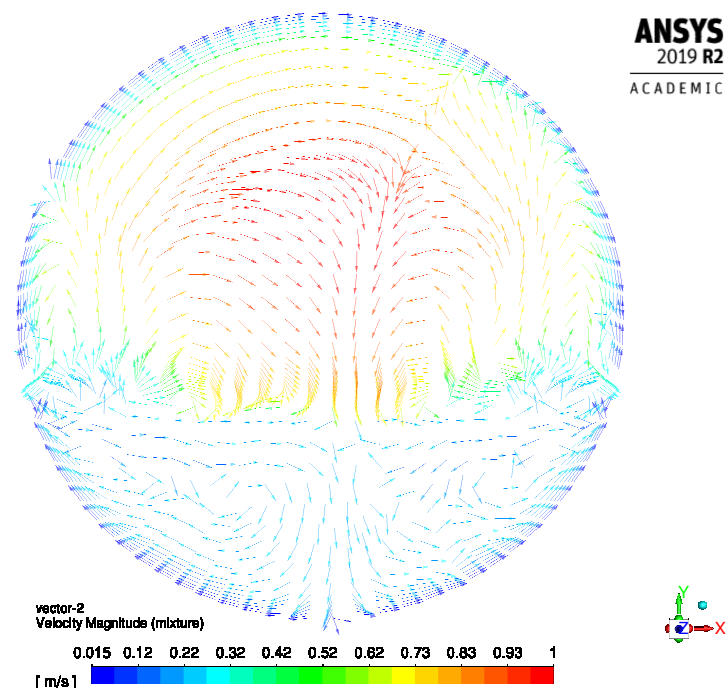Figure (5.8)   Turbulence Kinetic Energy Contours at the Half-Length Cross-Section

Figure (5.9)   Velocity Vectors Colored by the Velocity Magnitude at the Half-Length Cross-Section

Figure (5.11) shows the turbulent viscosity ratio at the half-length cross-section. The turbulent viscosity ratio, μ_t/μ, is directly proportional to the turbulent Reynolds number Re_t, that is shown in Figure (5.10). In high-Reynolds-number boundary layers, shear layers, and fully developed duct flows, Re_t is very large. The Generally, the turbulence parameters are set so that $1 < \mu_t/\mu < 10$. As can be seen from the figure, the maximum turbulent viscosity ratio is observed at the interface and on the gas side. Also, high values are observed in the water phase far away from the wall. The same behavior is observed for the turbulent Reynolds number.
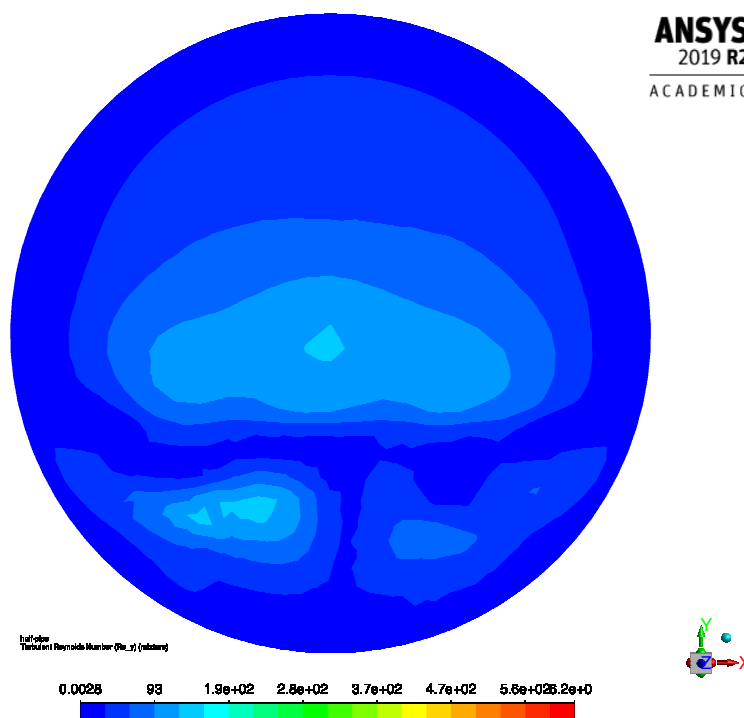

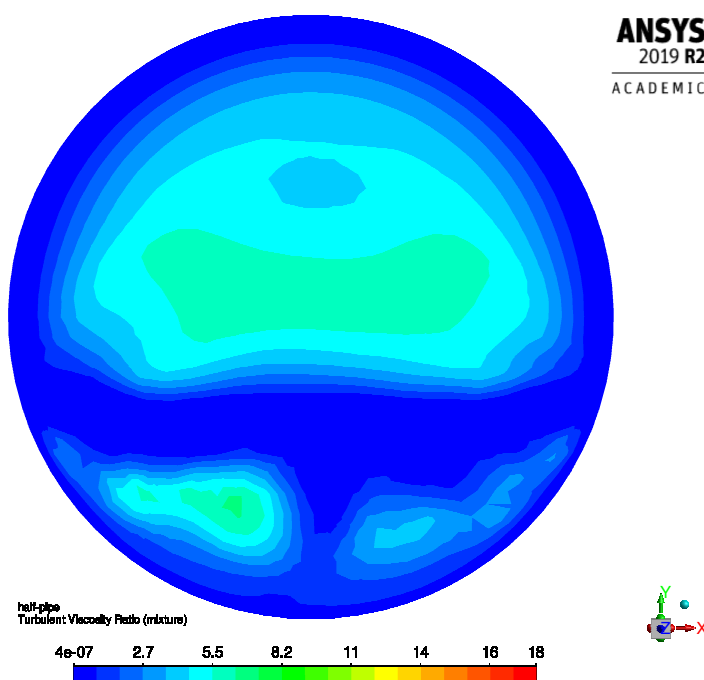Figure (5.10)   Turbulent Reynolds Number at the Half-Length Cross-Section

Figure (5.11)   Contours of the Turbulent Viscosity Ratio at the Half-Length Cross-Section

Figure (5.12a) shows the pressure gradient versus flow time. It is observed that the value of the pressure gradient becomes stable after the first turn-over time of the air phase. Figure (5.12b) provides a closer look at the diagram after stability is achieved. Some fluctuations can be seen; however, the range of these fluctuations is so small that these oscillations can be considered as negligible, and mean value can be determined for the pressure gradient.

Figure (5.13) and Figure (5.14) show the pressure and velocity of a point in the air phase versus the flow time, respectively, to show that the value of pressure gradient is determined for stable conditions in the air phase. Moreover, Figure (5.15) and Figure (5.16) are presented to show the stability of pressure and velocity in the water phase for the determination of the pressure drop. As can be observed, the velocity and pressure on the water side reach their stability after the first turn-over time of water.
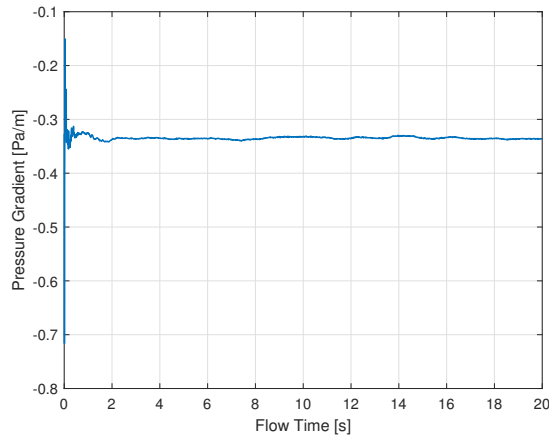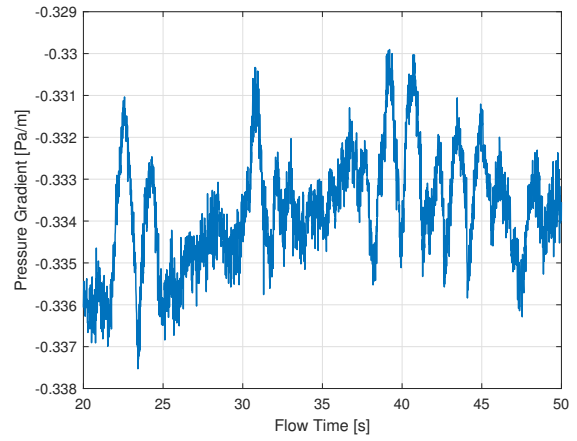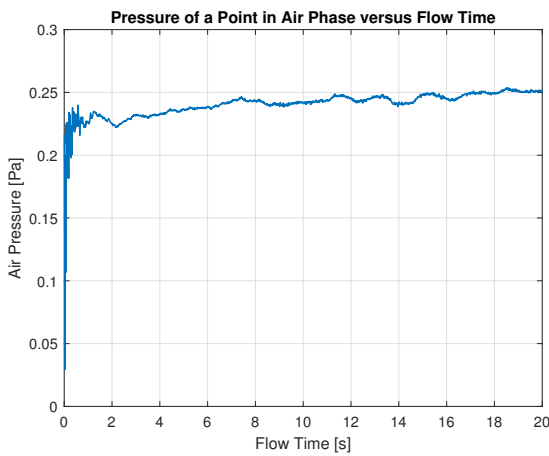
(a) 20[s]   (b) 20-50[s]
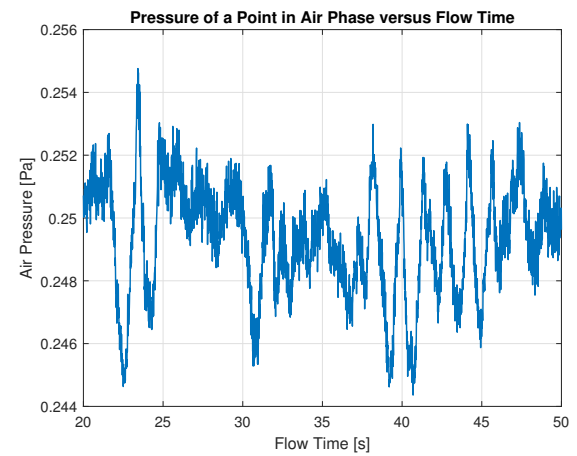
Figure (5.12)   Pressure Gradient versus Flow Time

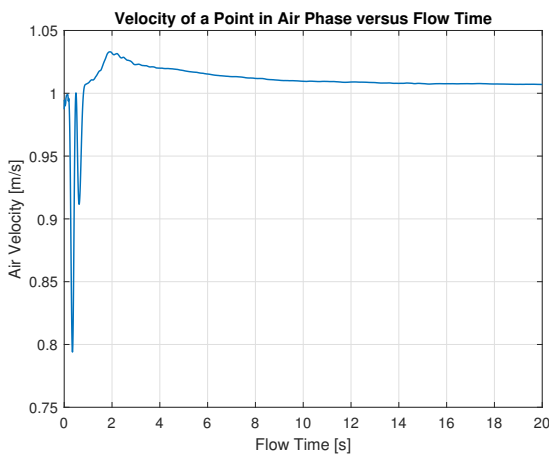(a) 20[s]   (b) 20-50[s]
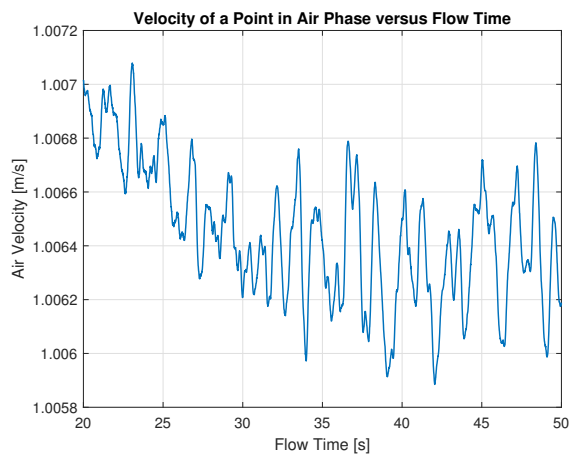
Figure (5.13)   Pressure of a Point in Air Phase versus Flow Time

(a) 20[s]   (b) 20-50[s]

Figure (5.14)   Velocity of a Point in Air Phase versus Flow Time
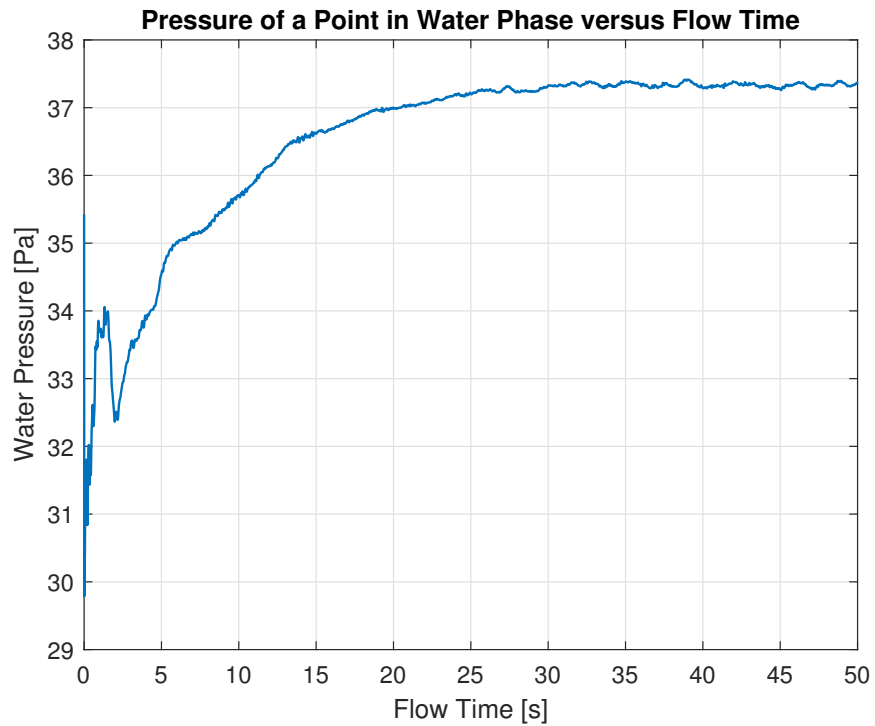
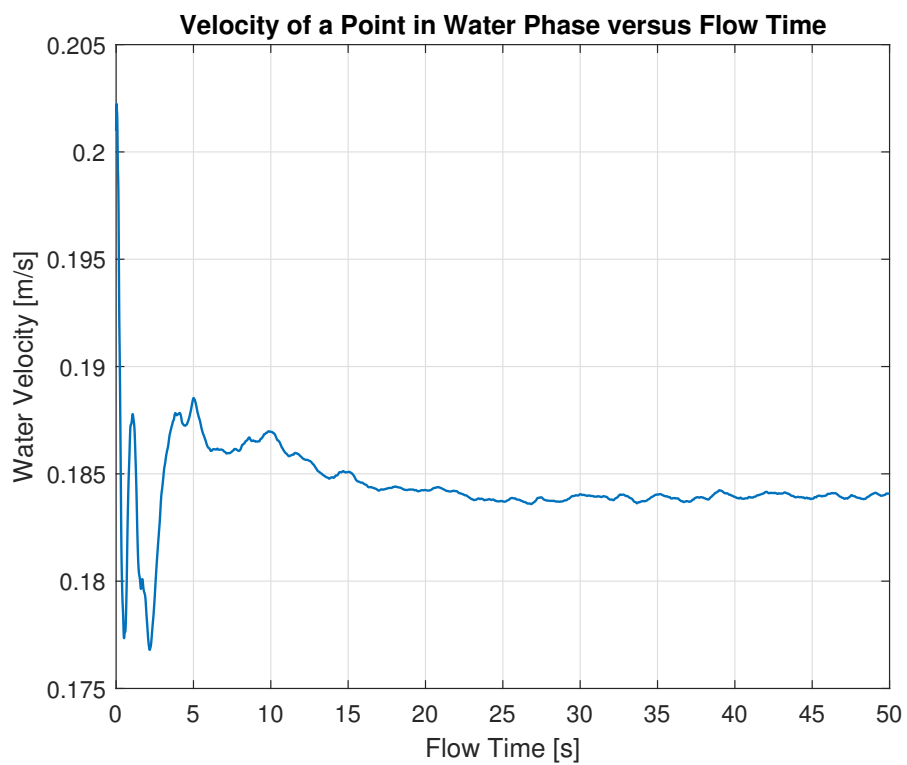Figure (5.15)   Pressure of a Point in Water Phase versus Flow Time Until 50[s]

Figure (5.16)   Velocity of a Point in Water Phase versus Flow Time Until 50[s]

A comparison is made between the pressure gradient value obtained from the numerical simulation and the measured experimental pressure gradient. Figure (5.17) shows this comparison of the pressure gradient versus void fraction for $J_L = 0.03[m/s]$. As can be seen, the deviation of numerical results from the experiments increases as the void fraction increases. The same behavior can be observed in Figure (5.18) for the superficial gas velocity at the same liquid superficial velocity. This deviation is also observed for other liquid superficial velocities. It should be mentioned that the trend of the pressure gradient versus the void fraction is close to an exponential function, whereas, the trend of the pressure gradient against the gas superficial velocity is a linear function.

Analogously, the same reasoning can be discussed for other liquid superficial velocities, as it is shown in Figure (5.19) and (5.20) for $J_L = 0.04[m/s]$ and in Figure (5.21) and (5.22) for $J_L = 0.05[m/s]$.

Comparing different liquid superficial velocities of $J_L = 0.03[m/s]$, $J_L = 0.04[m/s]$, and $J_L = 0.05[m/s]$, it is observed that the deviation from the experimental values for pressure gradient increases with increasing the liquid superficial velocity.

Figure (5.17)   Pressure Gradient Comparison between Numerical and Experimental Data versus Void Fraction ($J_L = 0.03[m/s]$)

Figure (5.18)   Pressure Gradient Comparison between Numerical and Experimental Data versus J_g ($J_L = 0.03[m/s]$)

Figure (5.19)   Pressure Gradient Comparison between Numerical and Experimental Data versus Void Fraction ($J_L = 0.04[m/s]$)
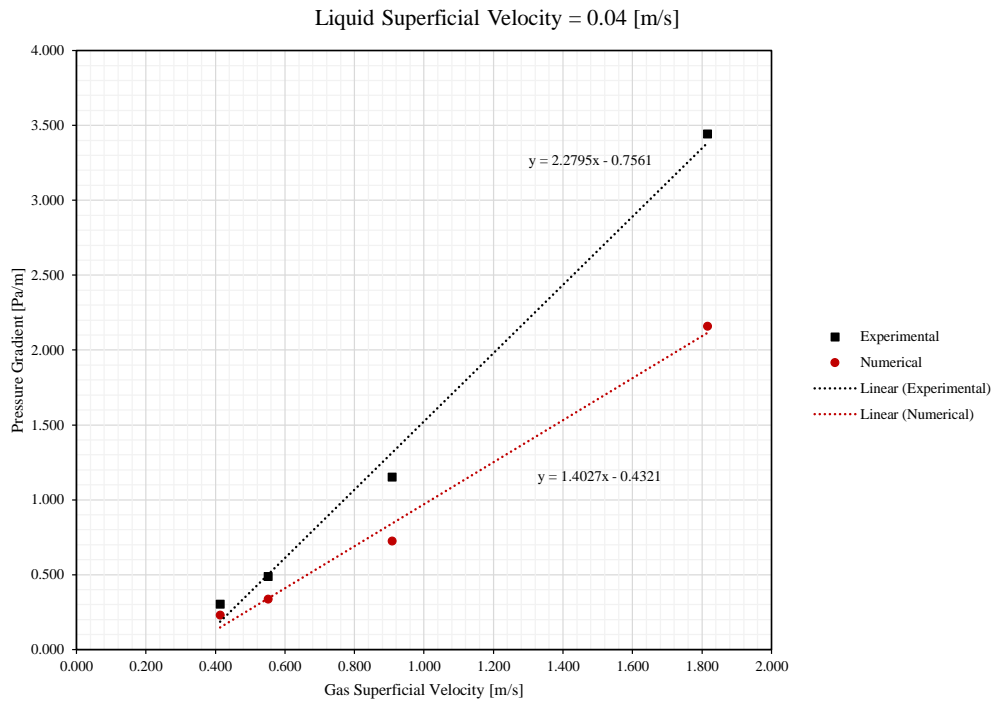
Figure (5.20)   Pressure Gradient Comparison between Numerical and Experimental Data versus J_g ($J_L = 0.04[m/s]$)
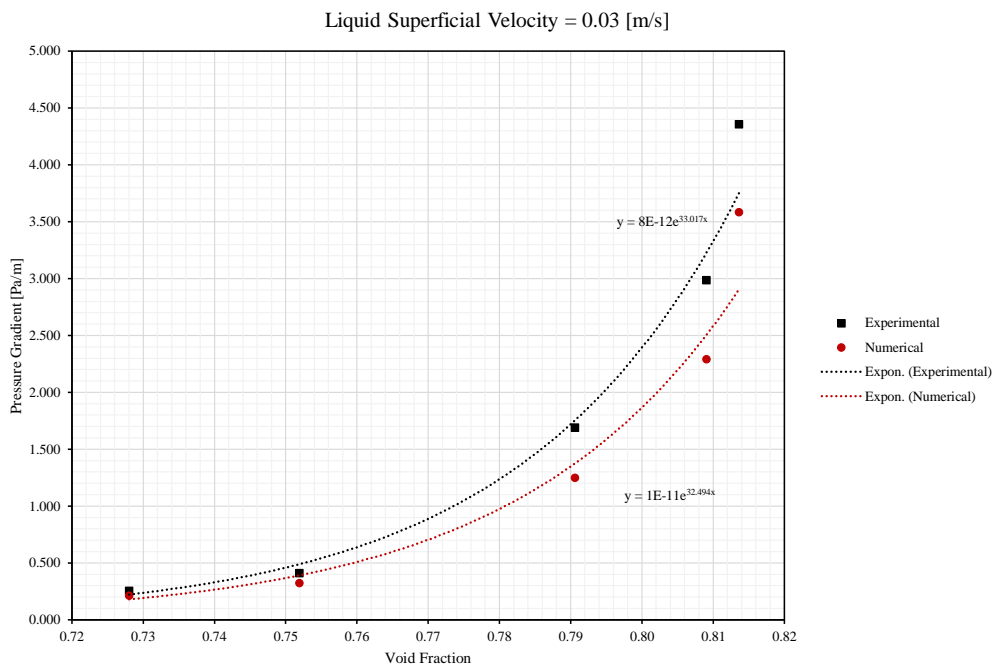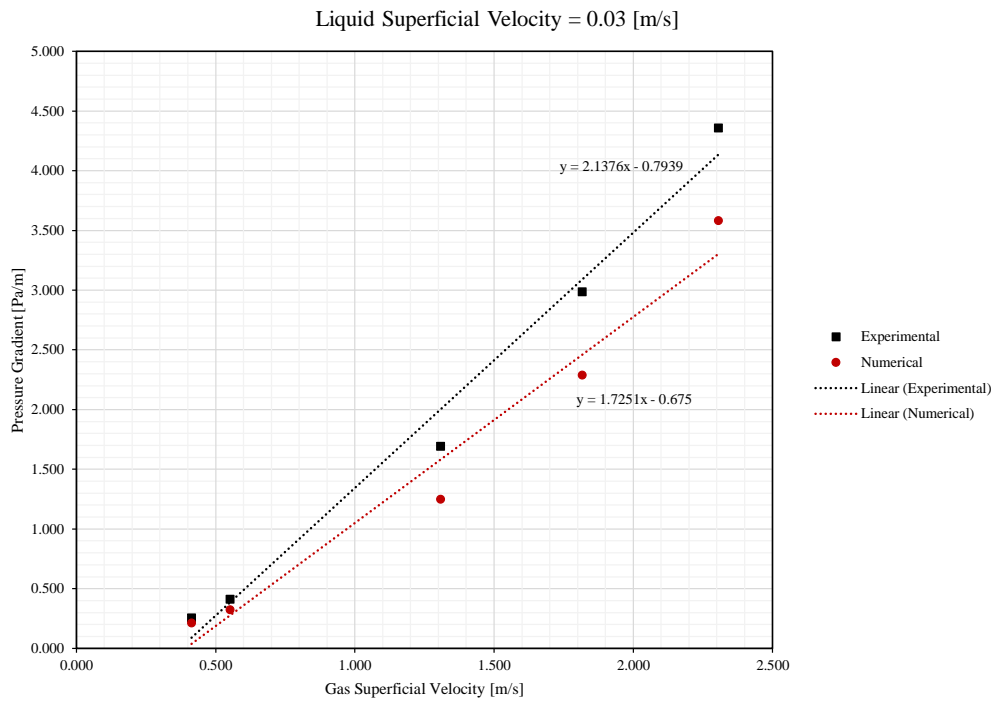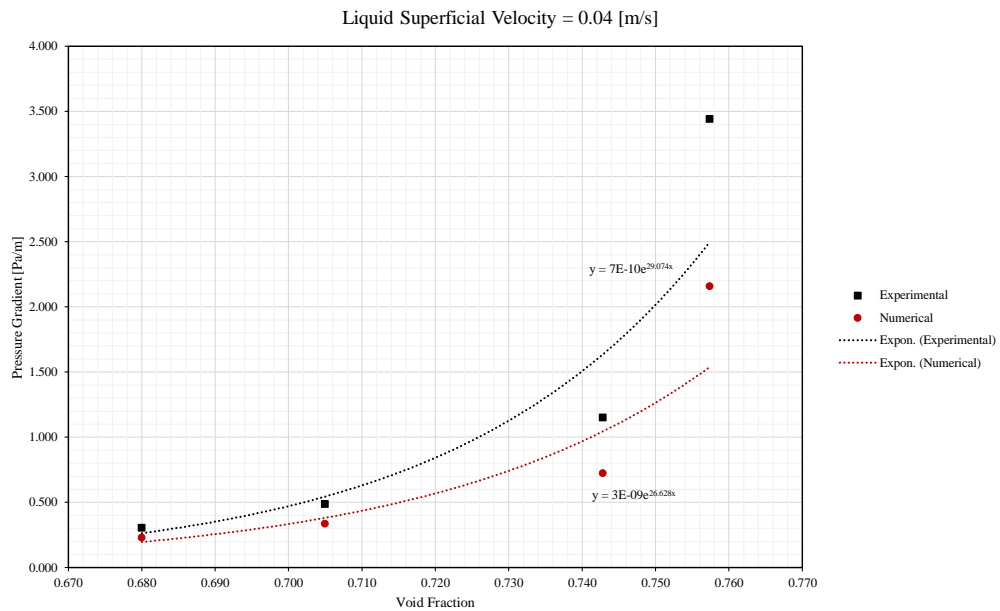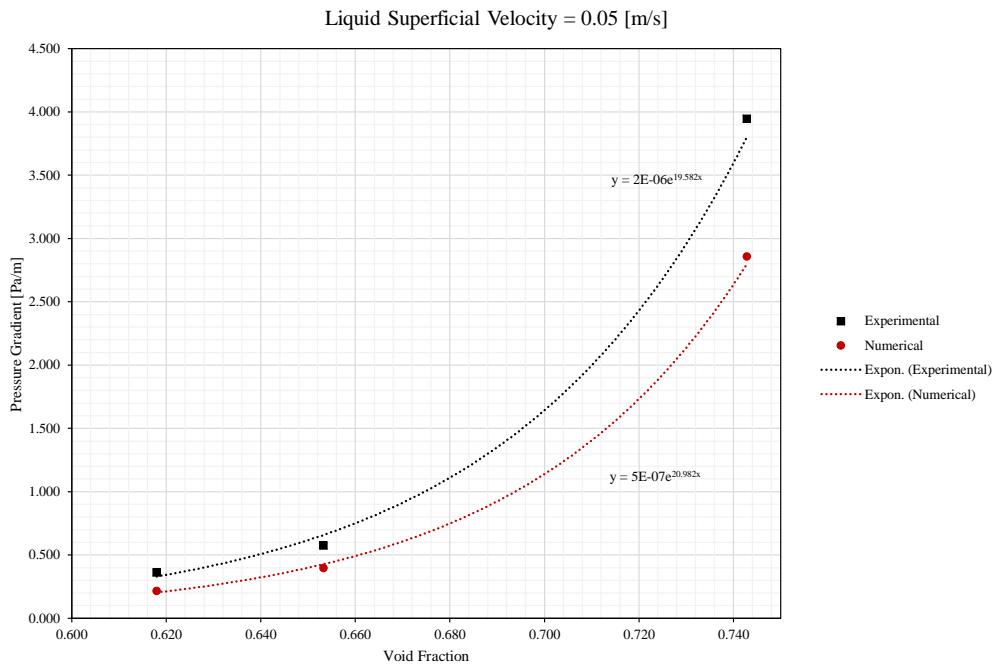

Figure (5.21)   Pressure Gradient Comparison between Numerical and Experimental Data versus Void Fraction ($J_L = 0.05[m/s]$)
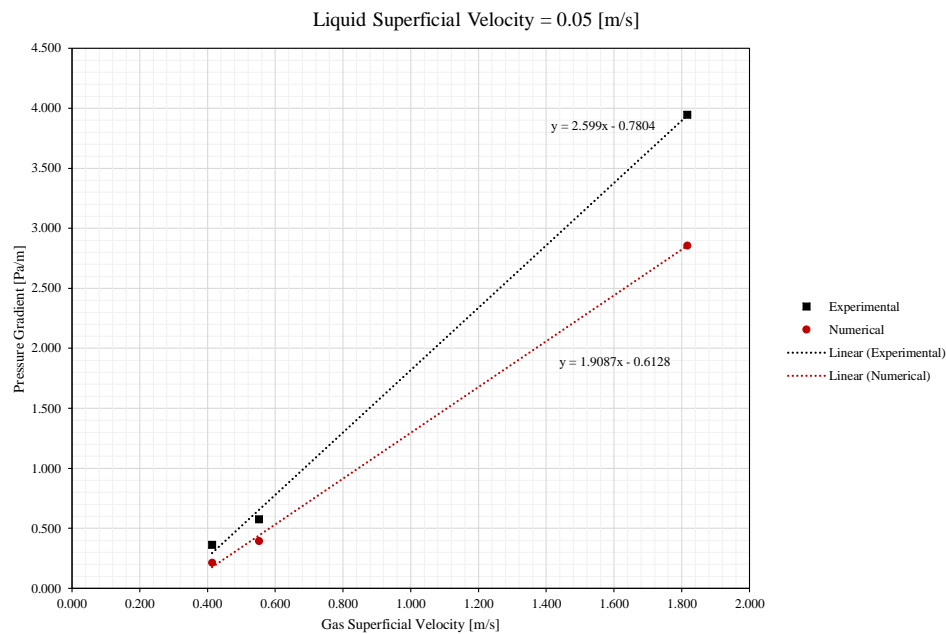
Figure (5.22)   Pressure Gradient Comparison between Numerical and Experimental Data versus J_g ($J_L = 0.05[m/s]$)

The mean absolute percentage error (MAPE) usually expresses accuracy as a percentage and is defined by the following formula,

$$M = \frac{100\%}{n} \sum_{t=1}^{n} \left| \frac{A_t - F_t}{A_t} \right| \tag{5.1}$$

where A_t is the actual value, and F_t is the forecast value. The difference between A_t and F_t is divided by the actual value A_t again. The absolute value in this calculation is summed for every predicted point in time and divided by the number of fitted points n. Multiplying by 100% makes it a percentage error. The values of the mean absolute percentage error are shown in Table (5.1) for different values of J_L. The overall value of MAPE for all the simulated points is equal to 28.91%.

Table (5.1)   Mean Absolute Percentage Error for Different Values of J_L

J_L[m/s]	MAPE[%]
0.03	21.044
0.04	32.522
0.05	33.162
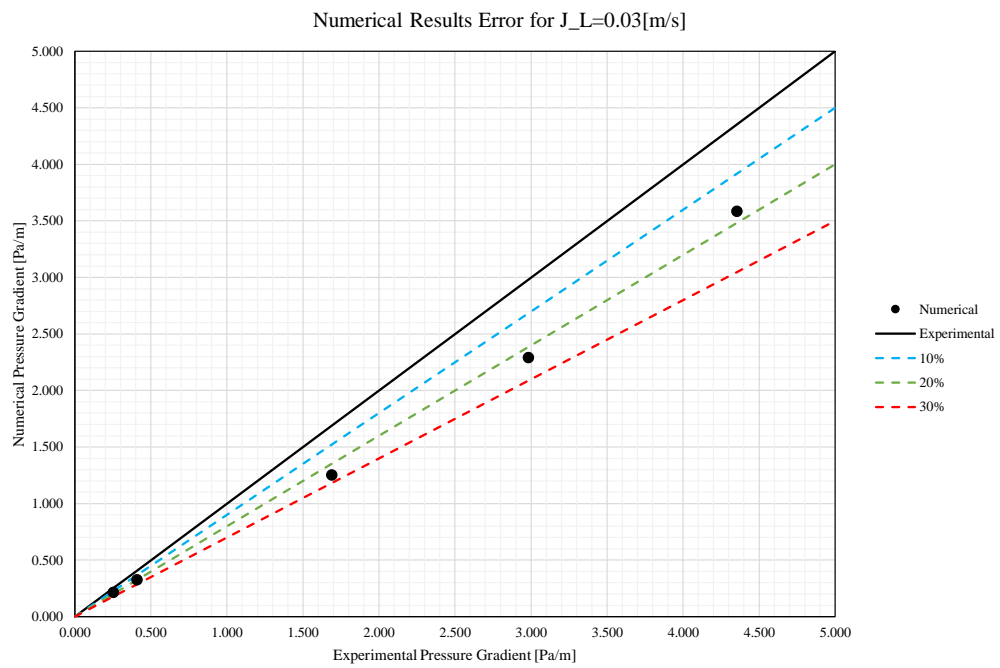
Figure (5.23)   Numerical Results Error ($J_L = 0.03[m/s]$)
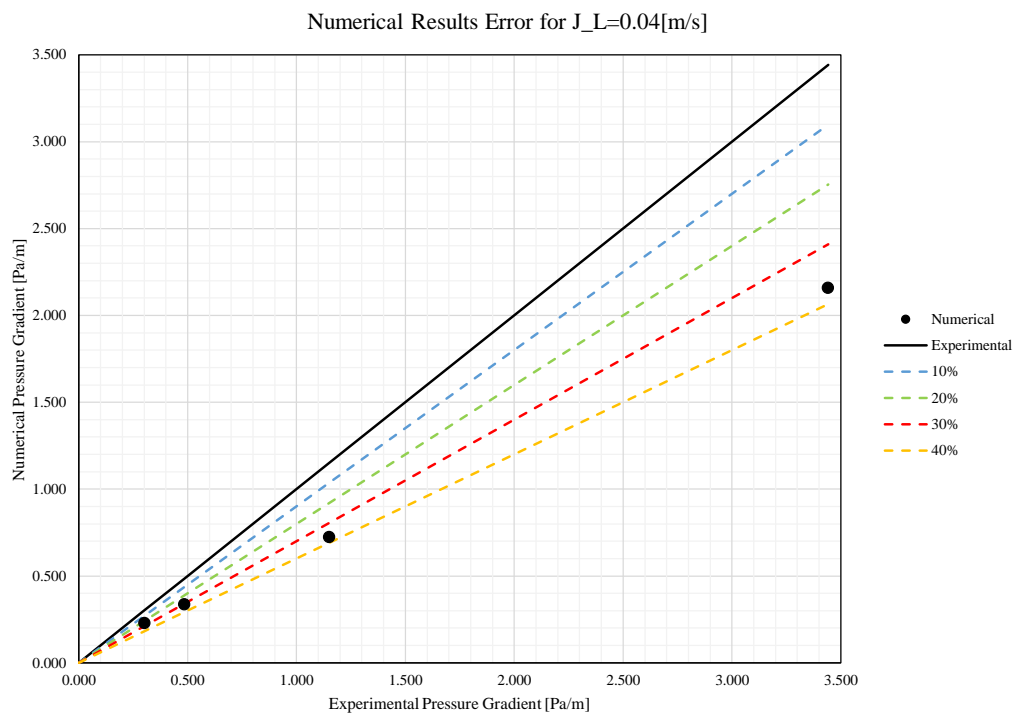
Figure (5.24)   Numerical Results Error ($J_L = 0.04[m/s]$)
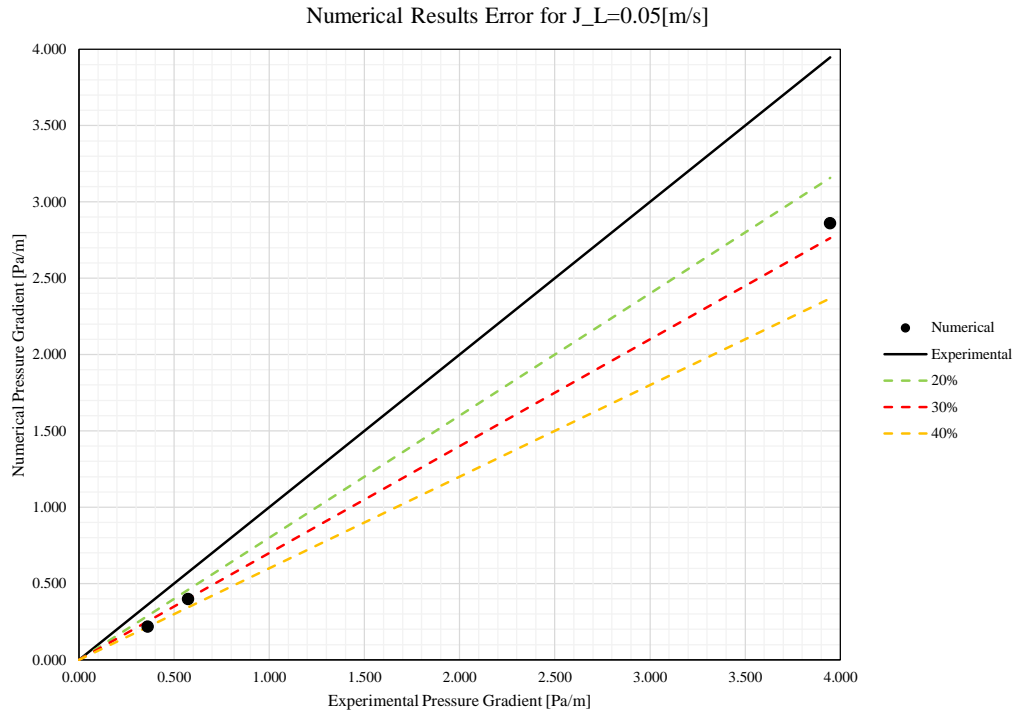
Figure (5.25)   Numerical Results Error ($J_L = 0.05[m/s]$)

5.2   Second Case Scenario - A More Realistic Analysis

5.2.1   Effect of Interface Mesh Refinement

The effect of moist air density is investigated for Experiment #10 (see Table (C.1)) with $J_l = 0.04[m/s]$, $J_g = 0.5513[m/s]$, $(dp/dz)_{experimental} = 0.486[Pa/m]$, and void fraction of 0.705. The mesh generated for this investigation is shown in Figure (4.3).

The results of the simulation show a slight decrease in the absolute percentage error of the pressure gradient of 0.31% under-prediction, which is insignificant.

5.2.2   Effect of Moist Air Density

The amount of water vapor in the air influences its density. Water vapor is relatively light compared to the diatomic Oxygen and diatomic Nitrogen, which are the dominant components in the air. When vapor content increases in the moist air, the amount of Oxygen and Nitrogen are decreased per unit volume and the density of the mixture decreases. Hence, dry air is denser than moist air.

Based on the specific volume of moist air, the moist air density can be calculated as

$$\rho = \frac{1}{v} = \frac{p}{R_a T}\frac{1+x}{1+x\frac{R_w}{R_a}} \tag{5.2}$$

where,
v= specific volume of moist air per mass unit of dry air and water vapor $[m^3/kg]$,
R_a= 286.9 - individual gas constant air [J/kg K],
R_w= 461.5 - individual gas constant water vapor [J/kg K],
x = humidity ratio [kg/kg],
p = pressure in the humid air [Pa].

The density of dry air can be expressed as

$$\rho_{dryair} = \frac{p}{R_a T} \tag{5.3}$$

Combining the two previous equations:

$$\rho = \rho_{dryair}\frac{1+x}{1+x\frac{R_w}{R_a}} \tag{5.4}$$

Since the gas constant ratio between water vapor and air is equal to $\frac{R_w}{R_a} = \frac{461.5J/kgK)}{286.9J/kgK} = 1.609$, The final form of Equation (5.4) becomes

$$\rho = \rho_{dryair}\frac{1+x}{1+1.609x} \tag{5.5}$$

The effect of mesh refinement is investigated for Experiment #10 (see Table (C.1)) with $J_l = 0.04[m/s]$, $J_g = 0.5513[m/s]$, $(dp/dz)_{experimental} = 0.486[Pa/m]$, and void fraction of 0.705. The mesh generated for this investigation is shown in Figure (4.2).

The results of the simulation show an increase in the absolute percentage error of the pressure gradient of 10.07% under-prediction which is a significant deviation from the experimental results (40.96% under-prediction of absolute percentage error compared to the experiments).

5.2.3   Combined Effects

Both effects of mesh refinement at the interface and moist air density is investigated on four cases of Experiment #9, #10, #12, and #15 with $J_L = 0.04[m/s]$. The comparison between experimental and numerical pressure gradient is shown in Figure (5.26). As it can be seen, the absolute percentage error difference between the combined effects and first case scenario is larger for lower void fractions and lower superficial gas velocities while this difference decreases for higher void fractions and higher superficial gas velocities where there is a higher difference between the superficial velocity of gas and liquid. MAPE for $J_L = 0.04[m/s]$ is equal to 38.16% of under-prediction, which has an increase of 5.64% compared to the previous model.
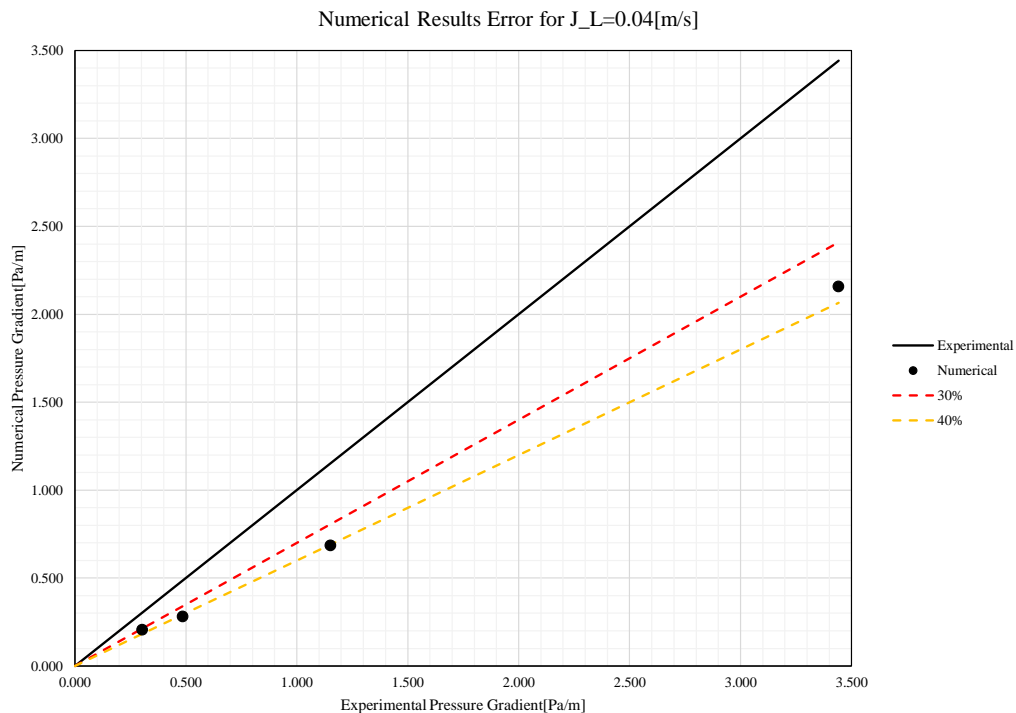
Figure (5.26) Numerical Results Error Considering Combined Effects ($J_L = 0.04[m/s]$)

The effects of interface mesh refinement and moist air density is investigated for the case of Experiment #8, where there is the maximum difference between the gas and liquid superficial velocities. The effect of mesh refinement at the interface results 2.63% over-prediction compared to the experiments which is very significant. When both effects were implemented in the simulation, a 13.22% under-prediction compared to the experimental pressure gradient with 4.57% closer results compared

to the first case scenario.

Comparing other flow characteristics in these three cases, the turbulent kinetic energy of the case with mesh refinement at the interface was higher than the case where no effects of moist air density or mesh refinement were considered. The turbulence kinetic energy of the case where both effects were taken into account was significantly higher than the other two. So an improvement of the prediction of the results is achieved for cases with higher difference between gas and liquid superficial velocities, while a large deviation from experiments is seen for pressure gradient where there is lower difference between gas and liquid superficial velocities as shown in Figure (5.27).

Liquid Superficial Velocity = 0.04 [m/s]
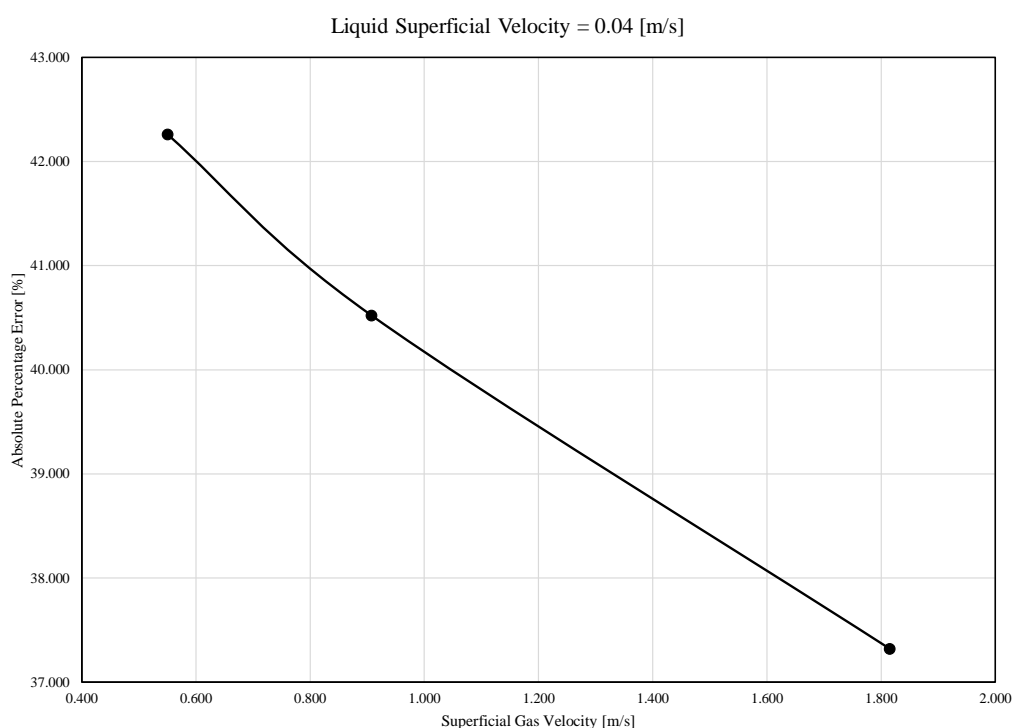
Figure (5.27)   Behaviour of Numerical Results Error versus Superficial Gas Velocity

5.3   Third Case Scenario - A More Realistic Analysis of Wavy Flow

The waves created in wavy flow are caused under conditions where the velocity of the gas is sufficient to cause waves to form; however, slower than that needed for rapid wave growth which causes the transition to slug or annular flow. These waves are generated when the pressure and shear work on a wave can overcome the viscous dissipation.

Taitel and Dukler (1976) worked on the transition from smooth to

wavy flow criteria. They implemented some approximations to Jefferys work which resulted the Equation (5.6) as the criterion for this transition,

$$u_G \geq \left[\frac{4\nu_L(\rho_L - \rho_G)g\cos\alpha}{s\rho_G u_L}\right]^{\frac{1}{2}} \tag{5.6}$$

In Equation (5.6), u_G and u_L are the superficial velocities of gas and liquid respectively, α is the inclination angle of the pipe, and s is a sheltering coefficient which Taitel and Dukler suggested should take a value of 0.01. The dimensionless form can be expressed as Equation (5.7),

$$K \geq \frac{2}{\sqrt{\widetilde{u_L}\widetilde{u_G}}\sqrt{s}} \tag{5.7}$$

where K is the product of the modified Froude and square root of the superficial Reynolds number of the liquid,

$$K^2 = F^2 Re_L^2 = \left[\frac{\rho_G u_G^2}{(\rho_L - \rho_G)Dg\cos\alpha}\right]\left[\frac{Du_L}{\nu_L}\right] \tag{5.8}$$

$\widetilde{u_L}$ and $\widetilde{u_G}$ can be calculated using the following equations:

$$\widetilde{u_L} = \frac{\widetilde{A}}{\widetilde{A_L}} \tag{5.9}$$

$$\widetilde{u_G} = \frac{\widetilde{A}}{\widetilde{A_G}} \tag{5.10}$$

where,

$$\widetilde{A_L} = 0.25\left[\pi - \cos^{-1}\left(2\widetilde{h_L} - 1\right) + \left(2\widetilde{h_L} - 1\right)\sqrt{1 - \left(2\widetilde{h_L} - 1\right)^2}\right] \tag{5.11}$$

$$\widetilde{A_G} = 0.25\left[\cos^{-1}\left(2\widetilde{h_L} - 1\right) - \left(2\widetilde{h_L} - 1\right)\sqrt{1 - \left(2\widetilde{h_L} - 1\right)^2}\right] \tag{5.12}$$

Analogous to the stratified flow, a simulation case is created for the wavy flow considering the work of Taitel and Duckler to determine the characteristics of the two-phase flow. Additional to the three-dimensional domain, a two-dimensional one is considered as well to accurately take into account the effects. Results will be discussed subsequently.

Conclusion

The present work focuses on the validation of the numerical simulation of two-phase stratified flow in horizontal pipes. Numerical simulations are performed using a 3D numerical domain where the interface tracking method Volume of Fluid (VOF) is coupled with the two-equation turbulence RANS model (SST k-ω). Several superficial gas and liquid velocities (i.e., several void fraction values) were simulated in adiabatic operating conditions. Numerical results show a good agreement with the experimental data collected at Politecnico di Milano. The results show a more significant difference at high superficial gas velocities as well as high superficial liquid velocities with mean absolute percentage error (MAPE) of around 29% on pressure gradient prediction. The comparison includes global quantities (e.g., pressure gradient) and visual behavior (e.g., the shape of the interface) confirming the capability of the numerical model to catch the main characteristics of the stratified fluid flow.

Furthermore, a sensitivity analysis is conducted, taking into account the density of moist air and a mesh refinement at the interface. An overall MAPE of 38% was obtained considering the combined effects which has an increase of 5% compared to the previous scenario. However, this significant difference is due to the deviation from experiments for low superficial gas velocities, while a better agreement was reached for high superficial gas velocities. Moreover, numerical results showed an improved agreement with experiments where the difference between gas and liquid superficial velocities was significant.

Additionally, wavy flow is simulated taken into account the sensitivity analysis performed for the stratified flow.

Potential future studies may include refinement at the interface using adaptive mesh in case of the wavy flow to investigate the shape of the interface.

Appendix A

VOF Model Implicit Formulation

When the implicit formulation is used, the volume fraction equation is discretized in the following manner:

$$\frac{\alpha_q^{n+1}\rho_q^{n+1} - \alpha_q^{n}\rho_q^{n}}{\Delta t}V + \sum_f \left(\rho_q^{n+1}U_f^{n+1}\alpha_{q,f}^{n+1}\right) = \left[S_{\alpha_q} + \sum_{p=1}^{n}\left(\dot{m}_{pq}\dot{m}_{qp}\right)\right]V$$

(A.1)

where:
$n+1=$ index for current time step
$n=$ index for previous time step
$\alpha_q^{n+1}=$ cell value of volume fraction at time step $n+1$
$\alpha_q^{n}=$ cell value of volume fraction at time step n
$\alpha_{q,f}^{n+1}=$ face value of the qth volume fraction at time step $n+1$
$U_f^{n+1}=$ volume flux through the face at time step $n+1$
$V=$ cell volume

Since the volume fraction at the current time step is a function of other quantities at the current time step, a scalar transport equation is solved iteratively for each of the secondary-phase volume fractions at each time step.

Face fluxes are interpolated using the chosen spatial discretization scheme. The implicit formulation can be used for both time-dependent and steady-state calculations.

Appendix B

VOF Model Explicit Schemes

B.1   The Donor-Acceptor Scheme

In the donor-acceptor approach, the standard interpolation schemes that are used in ANSYS Fluent are used to obtain the face fluxes whenever a cell is filled with one phase or another. When the cell is near the interface between two phases, a donor-acceptor scheme is used to determine the amount of fluid advected through the face. This scheme identifies one cell as a donor of an amount of fluid from one phase and another (neighbor) cell as the acceptor of that same amount of fluid and is used to prevent numerical diffusion at the interface. The amount of fluid from one phase that can be convected across a cell boundary is limited by the minimum of two values: the filled volume in the donor cell or the free volume in the acceptor cell.

The orientation of the interface is also used in determining the face fluxes. The interface orientation is either horizontal or vertical, depending on the direction of the volume fraction gradient of the phase within the cell and that of the neighbor cell that shares the face in question. Depending on the interface's orientation as well as its motion, flux values are obtained by pure upwinding, pure down winding, or some combination of the two.

When the donor-acceptor scheme is used, a time-dependent solution must be computed. Also, the donor-acceptor scheme can be used only with quadrilateral or hexahedral meshes.

B.2 The Compressive Interface Capturing Scheme for Arbitrary Meshes (CICSAM)

The compressive interface capturing scheme for arbitrary meshes (CIC-SAM), is a high-resolution differencing scheme. The CICSAM scheme is particularly suitable for flows with high ratios of viscosities between the phases. CICSAM is implemented in ANSYS Fluent as an explicit scheme and offers the advantage of producing an interface that is almost as sharp as the geometric reconstruction scheme.

B.3 The Compressive Scheme and Interface-Model-based Variants

The compressive scheme is a second order reconstruction scheme based on the slope limiter. Equation (B.1) is applicable to zonal discretization and the phase localized discretization, which use the framework of the compressive scheme.

$$\phi_f = \phi_d + \beta \nabla \phi_d \tag{B.1}$$

where
ϕ_f is the face VOF value
ϕ_d is the donor cell VOF value
β is the slope limiter value
$\nabla \phi_d$ is the donor cell VOF gradient value

The compressive scheme discretization depends on the selection of interface regime type.

B.4 Bounded Gradient Maximization (BGM)

The BGM scheme is introduced to obtain sharp interfaces with the VOF model, comparable to that obtained by the Geometric Reconstruction scheme. Currently, this scheme is available only with a steady-state solver and cannot be used for transient problems. In the BGM scheme, discretization occurs in such a way to maximize the local value of the gradient, by maximizing the degree to which the face value is weighted towards the extrapolated downwind value.

Appendix C

Obtained Data from the Experiments

Table (C.1) shows the experimental data obtained at the facility in Multiphase Thermo-Fluid Dynamics Laboratory at Politecnico di Milano.

These data were obtained for four values of the liquid superficial velocity by changing the gas superficial velocity. Pressure drop and water height were measured during the experiments.

Table (C.1)   Experimental Data obtained for the Range of Superficial Velocities

Superficial Velocities		Void Fraction	Pressure Gradient	Experiment
J_G [m/s]	J_L [m/s]	α [-]	$(-dp/dx)_E$ [Pa/m]	#
0.413	0.03	0.73	0.255	1
0.551	0.03	0.75	0.411	2
0.769	0.03	0.78	0.699	3
0.908	0.03	0.79	0.966	4
1.308	0.03	0.79	1.691	5
1.538	0.03	0.80	2.280	6
1.816	0.03	0.81	2.985	7
2.306	0.03	0.81	4.357	8
0.413	0.04	0.68	0.304	9
0.551	0.04	0.70	0.486	10
0.769	0.04	0.73	0.811	11
0.908	0.04	0.74	1.152	12
1.308	0.04	0.74	1.958	13
1.538	0.04	0.75	2.650	14
1.816	0.04	0.76	3.442	15
2.306	0.04	0.77	5.010	16
0.413	0.05	0.62	0.363	17
0.551	0.05	0.65	0.575	18
0.769	0.05	0.69	0.956	19
0.908	0.05	0.70	1.308	20
1.308	0.05	0.72	2.254	21
1.537	0.05	0.73	3.064	22
1.816	0.05	0.74	3.947	23
2.306	0.05	0.75	5.523	24
0.413	0.06	0.59	0.427	25
0.551	0.06	0.62	0.670	26
0.769	0.06	0.66	1.100	27
0.908	0.06	0.67	1.484	28
1.308	0.06	0.70	2.631	29
1.537	0.06	0.71	3.418	30
1.816	0.06	0.71	4.461	31
2.306	0.06	0.73	6.105	32

References

Akai, M., Inoue, A., Aoki, S., & Endo, K. (1980). A co-current stratified air-mercury flow with wavy interface. *International Journal of Multiphase Flow*, *6*(3), 173–190.

Ali, I. T. (2017). *Cfd prediction of stratified and intermittent gas-liquid twp-phase turbulent pipe flow using rans models* (Unpublished doctoral dissertation). The University of Manchester.

Al-Yaari, M. A., & Abu-Sharkh, B. F. (2011). Cfd prediction of stratified oil-water flow in a horizontal pipe. *Asian Transactions on Engineering*, *1*(5), 68–75.

Andritsos, N., & Hanratty, T. (1987). Interfacial instabilities for horizontal gas-liquid flows in pipelines. *International journal of multiphase flow*, *13*(5), 583–603.

Banerjee, R., & Isaac, K. (2003). Evaluation of turbulence closure schemes for stratified two phase flow. In *Asme 2003 international mechanical engineering congress and exposition* (pp. 689–705).

Bartosiewicz, Y., & Seynhaeve, J. (2006). Assessment of the neptune cfd platform to model the occurrence of instabilities in a stratified flow. In *Proceedings of the 10th international conference on multiphase flow in industrial plan (mfip'06)*.

Cerne, G., Petelin, S., & Tiselj, I. (2001). Coupling of the interface tracking and the two-fluid models for the simulation of incompressible two-phase flow. *Journal of computational physics*, *171*(2), 776–804.

Chinello, G. (2014). *Cfd modelling of stratified two phase flow for oil and gas transportation* (Unpublished master's thesis). Universita degli Studi di Pisa.

Chinello, G., Ayati, A. A., McGlinchey, D., Ooms, G., & Henkes, R. (2019). Comparison of computational fluid dynamics simulations and experiments for stratified air-water flows in pipes. *Journal of Fluids Engineering*, *141*(5), 051302.

Dabirian, R., Mansouri, A., Mohan, R., Shoham, O., Kouba, G., et al. (2015). Cfd simulation of turbulent flow structure in stratified gas/liquid flow and validation with experimental data. In *Spe annual technical conference and exhibition*.

de Sampaio, P. A., Faccini, J. L., & Su, J. (2008). Modelling of stratified gas–liquid two-phase flow in horizontal circular pipes. *International Journal of Heat and Mass Transfer*, *51*(11-12), 2752–2761.

Egorov, Y. (2004). Contact condensation in stratified steam-water flow. *Validation of CFD codes with PTS-relevant test cases-EVOL-ECORA D*, *7*.

Espedal, M. (1998). An experimental investigation of stratified two-phase pipe flow at small inclinations. *Norwegian University of Science and Technology (NTNU), Department of Applied Mechanics, Thermo-and Fluid Dynamics*.

Fabre, J., Masbernat, L., & Suzanne, C. (1987). Experimental data set no. 7: Stratified flow, part i: Local structure. *Multiphase Science and technology*, *3*(1-4).

Fernandino, M., & Ytrehus, T. (2006). Determination of flow sub-regimes in stratified air–water channel flow using ldv spectra. *International journal of multiphase*

flow, *32*(4), 436–446.

Gao, H., Gu, H.-Y., & Guo, L.-J. (2003). Numerical study of stratified oil–water two-phase turbulent flow in a horizontal tube. *International Journal of Heat and Mass Transfer*, *46*(4), 749–754.

Harlow, F. H., & Welch, J. E. (1965). Numerical calculation of time-dependent viscous incompressible flow of fluid with free surface. *The physics of fluids*, *8*(12), 2182–2189.

Hirt, C. W., & Nichols, B. D. (1981). Volume of fluid (vof) method for the dynamics of free boundaries. *Journal of computational physics*, *39*(1), 201–225.

Holmås, K., Nossen, J., Mortensen, D., Schulkes, R., Langtangen, H. P., et al. (2005). Simulation of wavy stratified two-phase flow using computational fluid dynamics (cfd). In *12th international conference on multiphase production technology*.

Issa, R. (1988). Prediction of turbulent, stratified, two-phase flow in inclined pipes and channels. *International Journal of Multiphase Flow*, *14*(2), 141–154.

Lo, S., Tomasello, A., et al. (2010). Recent progress in cfd modelling of multiphase flow in horizontal and near-horizontal pipes. In *7th north american conference on multiphase technology*.

Lockhart, R., & Martinelli, R. (1949). Proposed correlation of data for isothermal two-phase, two-component flow in pipes. *Chem. Eng. Prog*, *45*(1), 39–48.

Lorencez, C., Nasr-Esfahany, M., Kawaji, M., & Ojha, M. (1997). Liquid turbulence structure at a sheared and wavy gas-liquid interface. *International journal of multiphase flow*, *23*(2), 205–226.

Newton, C. H., & Behnia, M. (2000). Numerical calculation of turbulent stratified gas-liquid pipe flows. *International journal of multiphase flow*, *26*(2), 327–337.

Sanchis, A., Johnson, G. W., & Jensen, A. (2011). The formation of hydrodynamic slugs by the interaction of waves in gas–liquid two-phase pipe flow. *International Journal of Multiphase Flow*, *37*(4), 358–368.

Shoham, O., & Taitel, Y. (1984). Stratified turbulent-turbulent gas-liquid flow in horizontal and inclined pipes. *AIChE journal*, *30*(3), 377–385.

Sidi-Ali, K., & Gatignol, R. (2008). Cfd simulation of a stratified gas-liquid flow with and without the effect of gravity.

Strand, O. (1993). An experimental investigation of stratified two-phase flow in horizontal pipes. *University of Oslo, Oslo, Norway*.

Sussman, M., Smereka, P., & Osher, S. (1994). A level set approach for computing solutions to incompressible two-phase flow. *Journal of Computational physics*, *114*(1), 146–159.

Taitel, Y., & Dukler, A. E. (1976). A model for predicting flow regime transitions in horizontal and near horizontal gas-liquid flow. *AIChE journal*, *22*(1), 47–55.

Terzuoli, F., Galassi, M., Mazzini, D., & D'Auria, F. (2008). Cfd code validation against stratified air-water flow experimental data. *Science and Technology of Nuclear Installations*, *2008*.

Torres-Monzón, C. F. (2006). *Modeling of oil-water flow in horizontal and near horizontal pipes* (Unpublished doctoral dissertation). University of Tulsa.

Ullmann, A., & Brauner, N. (2006). Closure relations for two-fluid models for two-phase stratified smooth and stratified wavy flows. *International journal of multiphase flow*, *32*(1), 82–105.

Wallis, G. B., & Dodson, J. E. (1973). The onset of slugging in horizontal stratified air-water flow. *International Journal of Multiphase Flow*, *1*(1), 173–193.

Wilcox, D. C., et al. (1998). *Turbulence modeling for cfd* (Vol. 2). DCW industries La Canada, CA.